A&A, 707, A213 (2026)
https://doi.org/10.1051/0004-6361/202556654

Astronomy & Astrophysics

Multiwavelength properties of changing-state active galactic nuclei

I. The evolution of soft excess and X-ray continuum

Arghajit Jana[1,2,⋆], Claudio Ricci[3,1,4], Alessia Tortosa[5], George Dimopoulos[1], Benny Trakhtenbrot[6,7,8], Franz E. Bauer[9], Matthew J. Temple[10], Michael Koss[11,12], Kriti Kamal Gupta[13,14], Hsian-Kuang Chang[15], Yaherlyn Diaz[1], Dragana Illic[16,17], Kristína Kallová[1], and Elena Shablovinskaya[18]

[1] Instituto de Estudios Astrofísicos, Facultad de Ingeniería y Ciencias, Universidad Diego Portales, Av. Ejército Libertador 441, Santiago, Chile
[2] Department of Physics, SRM University-AP, Amaravati 522240, Andhra Pradesh, India
[3] Department of Astronomy, University of Geneva, ch. d'Ecogia 16, 1290 Versoix, Switzerland
[4] Kavli Institute for Astronomy and Astrophysics, Peking University, Beijing 100871, PR China
[5] INAF-Osservatorio Astronomico di Roma, via di Frascati 33, I-00078 Monte Porzio Catone, Italy
[6] School of Physics and Astronomy, Tel Aviv University, Tel Aviv 69978, Israel
[7] Max-Planck-Institut für extraterrestrische Physik, Gießenbachstraße 1, 85748 Garching, Germany
[8] Excellence Cluster ORIGINS, Boltzmannsstraße 2, 85748 Garching, Germany
[9] Instituto de Alta Investigación, Universidad de Tarapacá, Casilla 7D Arica, Chile
[10] Centre for Extragalactic Astronomy, Department of Physics, Durham University, South Road, Durham DH1 3LE, UK
[11] Eureka Scientific, 2452 Delmer Street Suite 100, Oakland, CA 94602-3017, USA
[12] Space Science Institute, 4750 Walnut Street, Suite 205, Boulder, CO 80301, USA
[13] STAR Institute, Liège Université, Quartier Agora – Allée du six Août, 19c, B-4000 Liège, Belgium
[14] Sterrenkundig Observatorium, Universiteit Gent, Krijgslaan 281 S9, B-9000 Gent, Belgium
[15] Institute of Astronomy, National Tsing Hua University, Hsinchu 300044, Taiwan
[16] Department of Astronomy, Faculty of Mathematics, University of Belgrade, Studentski trg 16, 11000 Belgrade, Serbia
[17] Hamburger Sternwarte, Universitat Hamburg, Gojenbergsweg 112, D-21029 Hamburg, Germany
[18] Humboldt Research Fellow, Max-Planck-Institut für Radioastronomie, Auf dem Hügel 69, Bonn D-53121, Germany

Received 29 July 2025 / Accepted 8 January 2026

ABSTRACT

Changing-state active galactic nuclei (CSAGNs) exhibit rapid variability; their mass accretion rates can change by several orders of magnitude in a few years. This provides us with a unique opportunity to study the evolution of the inner accretion flow almost in real time. Here we used over 1000 observations to study the broadband X-ray spectra of a sample of five CSAGNs, spanning three orders of magnitude in Eddington ratio ($\lambda_{\rm Edd}$), using phenomenological models to trace the evolution of key spectral components. We derive several fundamental parameters, such as the photon index, soft excess strength, reflection strength, and luminosities of the soft excess and primary continuum. We find that the soft excess and primary continuum emissions show a very strong positive correlation ($p \ll 10^{-10}$), suggesting a common physical origin. The soft excess strength does not show any dependence on the reflection parameter, suggesting that in these objects the soft excess is not dominated by a blurred ionized reflection process. On the other hand, the strength of the soft excess is found to be strongly positively correlated with the Eddington ratio ($p \ll 10^{-10}$), and we find that the soft excess vanishes below $\log \lambda_{\rm Edd} \sim -2.5$. Moreover, we find a clear V-shaped relation for $\Gamma - \lambda_{\rm Edd}$, with a break at $\log \lambda_{\rm Edd} = -2.47 \pm 0.09$. Our findings indicate a change in the geometry of the inner accretion flow at low Eddington ratios, and that the soft excess is primarily produced via warm Comptonization.

Key words. accretion, accretion disks – galaxies: active – galaxies: nuclei – quasars: supermassive black holes – X-rays: galaxies

1. Introduction

Active galactic nuclei (AGNs) are powered by accreting supermassive black holes (SMBHs) located at galaxy centers (Rees 1988). Matter from the surrounding medium accretes onto the black hole through a geometrically thin, optically thick accretion disk. As the material spirals inward, its gravitational potential energy is efficiently converted into radiation, which is emitted across the entire electromagnetic spectrum. The inner accretion flow consists of a geometrically thin, optically thick disk and a compact X-ray corona. Such a disk emits mainly in UV/optical, thus producing the characteristic big blue bump in the spectral energy distribution (SED; Shakura & Sunyaev 1973; Malkan & Sargent 1982; Koratkar et al. 1995), while inverse Compton scattering of the UV photons by hot electrons in the corona produces a power-law X-ray continuum (Sunyaev & Titarchuk 1980; Haardt & Maraschi 1991). Additional excess emission above the power-law continuum is commonly observed below ∼1−2 keV, and is known as the soft excess (SE; Singh et al. 1985; Arnaud et al. 1985). The origin of this SE remains the subject of debate. Two primary scenarios have been proposed to explain the SE: (i) ionized

⋆ Corresponding author: arghajit.jana@mail.udp.cl

reflection from the inner accretion disk (Crummy et al. 2006; Walton et al. 2013; Dauser et al. 2014) and (ii) thermal Comptonization in a warm corona (Done et al. 2012; Petrucci et al. 2013). In the ionized reflection model, SE arises from blurred ionized reflection, where fluorescent lines from reprocessed X-ray emission are smeared due to the strong gravitational field near the SMBH (e.g., Ross & Fabian 2005; García & Kallman 2010; Dauser et al. 2016; Ding et al. 2024). In contrast, the warm corona model attributes the SE to thermal Comptonization of seed photons from the AD in an optically thick, warm plasma (e.g., Magdziarz et al. 1998; Petrucci et al. 2018), which is distinct from the hot corona ($kT_{\rm h} \sim 50-100$ keV; $\tau_{\rm h} \lesssim 1$) responsible for the primary X-ray power-law emission. The warm corona is typically characterized by an electron temperature of $kT_{\rm w} \sim 0.1-0.2$ keV and an optical depth of $\tau_{\rm w} \sim 10-20$ (Petrucci et al. 2018). A hybrid origin involving both components is also proposed (García et al. 2019; Laha et al. 2022; Xiang et al. 2022; Chen et al. 2025).

Due to the high mass of the SMBHs ($M_{\rm BH} \sim 10^6-10^9\,M_\odot$), the timescales expected for significant optical/UV variations in AGNs are expected to be $\sim 10^4-10^7$ yr (e.g., Frank et al. 2002; Netzer 2013). Thus, major changes in accretion disk (AD) emission are in principle not expected to be observable on timescales of a few years. This limitation has been overcome by studying large samples of AGNs, which includes objects with very different accretion rates. This can offer some insights into the inner accretion flow dynamics across a wide range of accretion rates (e.g., Krolik 1999; Netzer 2013). A complementary approach involves studying black hole X-ray binaries (BHXBs), which can transition between different accretion states on timescales of months, allowing a detailed investigation of accretion physics (e.g., Remillard & McClintock 2006; Done et al. 2007). Despite the large difference in mass, AGNs might have similar accretion mechanisms to BHXBs (e.g., Merloni et al. 2003; McHardy et al. 2006), as suggested by their comparable spectral and timing properties (e.g., Sobolewska et al. 2011). However, some observational differences remain. For example, AGNs exhibit a soft X-ray excess (SE) below $\sim 1-2$ keV not seen in BHXBs (Gierliński & Done 2004; Done et al. 2012; Ricci et al. 2017), for which the soft X-ray emission is often dominated by the accretion disk (e.g., Remillard & McClintock 2006). Additionally, AGNs display a dichotomy in radio loudness: Some sources launch powerful relativistic jets and others remain radio quiet, even at similar accretion rates (e.g., Sikora et al. 2007, see also Svoboda et al. 2017), while BHXBs show tighter correlations between jet activity and accretion state (Merloni et al. 2003; Fender & Belloni 2004).

Changing-state AGNs (CSAGNs) provide a unique opportunity to probe AGN accretion physics as their accretion rates can evolve by $\sim 1-2$ orders of magnitude within weeks to years (e.g., MacLeod et al. 2016; Ruan et al. 2019; Trakhtenbrot et al. 2019; Temple et al. 2023; Ricci et al. 2021; Ricci & Trakhtenbrot 2023). In UV/optical wavebands, CSAGNs switch between type 1 states, with broad emission lines (BELs), and type 2 states, without broad emission lines, on timescales ranging from a few months to a few years (Stern et al. 2018; Noda & Done 2018). These transitions are primarily attributed to significant changes in the accretion rate (Sheng et al. 2017; Noda & Done 2018; Ricci & Trakhtenbrot 2023; Jana et al. 2025).

Accretion rate changes in CSAGNs are attributed to disk instabilities (Noda & Done 2018) or external perturbation, such as tidal disruptions (Merloni et al. 2015; Ricci et al. 2020). Noda & Done (2018) suggested that the SE ionizes the BLR, leading to BELs in type 1 states; however, in type 2 states, as SE intensity diminishes, BELs disappear. In Mrk 1018, the CS transition was accompanied by a decrease in the Eddington ratio ($\lambda_{\rm Edd} = L_{\rm bol}/L_{\rm Edd}$) from ~0.08 to ~0.006, while the primary X-ray continuum (PC) and SE flux decreased by factors of ~7 and ~60, respectively. SE evolution has been observed in other CSAGNs (e.g., Laha et al. 2022; Tripathi & Dewangan 2022; Layek et al. 2024), resembling soft to hard state transitions in BHXBs around $\lambda_{\rm Edd} \sim 0.01-0.02$ (e.g., Maccarone 2003; Done et al. 2007; Yang et al. 2015). A systematic study of optically identified CLAGNs using *Swift*/BAT light curves by Temple et al. (2023) showed significant 14–195 keV flux changes in most CLAGNs during optical transitions, suggesting these events are largely driven by accretion state changes. Using long-term optical and X-ray quasi-simultaneous observations, Jana et al. (2025) confirmed this picture, finding that transitions typically occur around $\lambda_{\rm Edd}^{\rm tr} \sim 0.01$, consistent with other studies (e.g., Ruan et al. 2019; Ai et al. 2020),

The inner accretion geometry is expected to change at a few percent of the Eddington ratio (e.g., Esin et al. 1997; Yuan & Narayan 2014). This change is thought to be imprinted on the observed V-shaped photon index (Γ)–$\lambda_{\rm Edd}$ relation (e.g., Shemmer et al. 2006; Emmanoulopoulos et al. 2012; Trakhtenbrot et al. 2017; She et al. 2018; Peca et al. 2025, and references therein). At $\lambda_{\rm Edd} > 0.01$, the accretion disk likely extends close the innermost stable circular orbit (ISCO), accompanied by a compact X-ray corona. At $\lambda_{\rm Edd} < 0.01$, the disk is thought to be truncated at larger radii, possibly due to evaporation of the inner region. This creates a hot radiatively inefficient advective flow (RIAF) that replaces the inner disk and may increase the size of the X-ray emitting region (Chakrabarti & Titarchuk 1995; Reis & Miller 2013; Yuan & Narayan 2014; Yang et al. 2015). Although, the exact geometry of the X-ray emitting region is still debated. The positive $\Gamma - \lambda_{\rm Edd}$ correlation at high accretion rates ($\lambda_{\rm Edd} > 0.01$) can be explained by thermal Comptonization, where disk photons are up-scattered in the corona, producing a power-law X-ray spectrum. As $\lambda_{\rm Edd}$ rises, the increased photon flux cools the corona, resulting in a softer spectrum (higher Γ). Additionally, a higher Eddington ratio increases the compactness of the coronae, and enhances the pair production (Ricci et al. 2018). As the source is expected to remain below the pair line, the increase in compactness would result in a decrease in $kT_{\rm e}$, leading to softer spectra. At lower accretion rates ($\lambda_{\rm Edd} < 0.01$), synchrotron emission from the RIAF or jet base may dominate as the primary seed photons. With decreasing $\lambda_{\rm Edd}$, the density and optical depth of the flow decrease, which would weaken the synchrotron self-absorption. This would lead to the production of more seed photons with respect to the power dissipated in the flow, leading to a softening of the spectrum (Zdziarski et al. 2014; Yang et al. 2015).

Therefore, CSAGNs provide a unique opportunity to probe the inner accretion flow evolution on observable timescales. For this paper we studied the broadband X-ray properties of five CSAGNs to understand how the inner accretion flow with the accretion rates. Additionally, we also explored the evolution of the SE emission to understand its nature and origin. In forthcoming publication, we will investigate the UV to X-ray spectral energy distributions (SEDs) of CSAGNs to characterize the disk-corona connection across Eddington ratios.

The current paper is organized as follows. Section 2 describes the sample selection, observations, and data reduction. Section 3 presents the analysis methods. Section 4 discusses our findings. Finally, we summarize the results in

Table 1. General properties of the sample of CSAGNs.

No.	Name	BAT ID	RA	Dec	z	d_L (Mpc)	$\log(M_{BH}/M_\odot)$	Ref
(1)	(2)	(3)	(4)	(5)	(6)	(7)	(8)	(9)
1	NGC 1566	216	65.002	–54.938	0.0047	17.9	6.83	A
2	NGC 2617	1327	128.912	–4.088	0.0142	61.5	7.32 ± 0.08	B
3	Mrk 590	116	33.639	–0.767	0.026	115.7	7.57	A
4	Mrk 1018	106	31.567	–0.291	0.042	188.5	7.81	A
5	IRAS 23226–3843	1194	351.359	–38.471	0.035	158.7	7.83	A

Notes. Columns: (2) Common name of the sources, (3) BAT ID, (4) & (5) Source position in J2000 epoch, (6) Redshift of the source, (7) Luminosity distance of the sources, (8) Black hole mass, (9) References for mass. Mass reference: (A) Koss et al. (2022b), (B) Feng et al. (2021).

Section 5. Throughout, we adopt a ΛCDM cosmology with $H_0 = 70\,\mathrm{km\,s^{-1}\,Mpc^{-1}}$, $\Omega_M = 0.3$, and $\Omega_\Lambda = 0.7$.

2. Sample, observations, and data

2.1. Sample selection

The primary aim of this work is to investigate the soft X-ray properties of CSAGNs, especially the SE. We drew our sample of CSAGNs from the work of Jana et al. (2025), who studied a sample of optically identified CLAGNs (Temple et al. 2023) selected from the BAT AGN Spectroscopic Survey (BASS) project[1]. We selected our sample based on two criteria. First, the CSAGNs showed both type 1 and type 2 spectral states in the optical regime in post-2000. Second, the CSAGNs have simultaneous multi-epoch and multiwavelength observations, from UV/optical to X-rays. Based on this, we found nine CSAGNs that meet both criteria. However, we excluded four sources from our sample, namely NGC 1365, NGC 3516, NGC 4151, and NGC 5548, due to the presence of warm absorbers and disk winds (Risaliti et al. 2005, 2009; Mehdipour et al. 2022a; Beuchert et al. 2017; Edelson et al. 2017; Mehdipour et al. 2022b). The presence of warm absorbers and/or disk winds would have made it difficult to infer the intrinsic SE properties. The final sample consisted of five CSAGNs, namely NGC 1566, NGC 2617, Mrk 590, Mrk 1018, and IRAS 23226–3843. NGC 1566 showed signatures of possible outflows in two observations, which we did not consider for our study. These sources are unobscured, and hence absorption is unlikely to affect the SE. Some of the main properties of these five sources are presented in Table 1.

For our sample, we primarily adopted black hole masses from the BASS data release 2 (DR2) catalog, which estimates the M_{BH} in a consistent way using uniform scaling relations and fitting procedures for the broad and narrow components (see Koss et al. 2022a, for details). The only exception is NGC 2617, for which we used the reverberation mapping estimation of M_{BH} (Feng et al. 2021). In BASS DR2, the M_{BH} for NGC 1566, Mrk 590, and Mrk 1018 were estimated using single-epoch measurements based on broad emission lines, while the mass for IRAS 23226–3843 was obtained via the M_{BH}–σ_* relation (Koss et al. 2022b). Although different mass estimations exist in the literature for these sources, we relied on the BASS DR2 values wherever available to maintain consistency across the sample. We note that these masses are not homogeneous in the sense of being measured at comparable luminosity or λ_{Edd}, and systematic uncertainties related to accretion state may affect single epoch virial estimates (see, e.g., Panda & Śniegowska 2024).

2.2. Data reduction process

For the present work we utilized the data obtained from *Swift* (Burrows et al. 2005), *XMM-Newton* (Jansen et al. 2001), *Suzaku* (Koyama et al. 2007; Takahashi et al. 2007), and *NuSTAR* (Harrison et al. 2013). The observation log is presented in Table A.1.

2.2.1. Swift

Swift observed the five CSAGNs in our sample 1021 times between 2005 and 2024. We used all available *Swift*/XRT observations, taken in both photon-counting and window-timing modes. To improve the signal-to-noise ratio for spectral analysis and enable detection of SE emission, we combined observations under two conditions: (i) consecutive epochs with fluxes consistent within 10% and total exposure ≥3000 s and S/N ≥ 20; or (ii) when the next observation was more than 6 months apart. The 0.5−10 keV spectra were generated using the online tools from the UK Swift Science Data Centre[2] (Evans et al. 2009). Source spectra were extracted from circular regions with radii between 28″.3 and 59″.0, depending on source brightness, and background spectra from a 260″.0 region (see Vasudevan & Fabian 2007). We rebinned the spectra with a minimum of one count per bin using the GRPPHA task.

Swift/UVOT provides data in three optical (V, B, U) and three UV (UVW1, UVM2, UVW2) filters. We reduced the level 2 image files and performed photometry with UVOTSOURCE, adopting a 5″ circular aperture centered on the source and a 20″ background region free of contaminating sources. This yielded source and background counts, fluxes, and magnitudes. UVOT observations obtained simultaneously with XRT exposures were merged for consistency. We estimated the host-galaxy corrected UV fluxes by subtracting the host galaxy fluxes from Gupta et al. (2024).

2.2.2. XMM–Newton

We analyzed a total 42 *XMM–Newton*-EPIC/PN observations of our five CSAGNs in the 0.5−10 keV energy range. Data reduction was performed using the Standard Analysis Software (SAS) version 20.0.0. The raw PN event files were processed with the EPCHAIN task, and particle background flares in the 10−12 keV

[1] https://www.bass-survey.com/

[2] https://www.swift.ac.uk/user_objects/

energy range were inspected. Good time intervals (GTIs) were generated using the TABGTIGEN task.

Using the ESPECGET task, source and background spectra were extracted from a circular region with a radius of 30″, centered on the position of the optical counterpart and away from the X-ray source on the same CCD, respectively. With the EPATPLOT task, we checked for pileup. We removed the pileup by adjusting the inner and outer radii of the annular region for the source extraction. The response files were generated using the SAS tasks RMFGEN and ARFGEN. We rebinned the spectra with a minimum of 20 counts per bin using the GRPPHA task.

2.2.3. NuSTAR

We utilized a total of 22 *NuSTAR* (Harrison et al. 2013) observations for our sample of CSAGNs in the 3−78 keV energy range. Using NuSTAR Data Analysis Software `NuSTARDAS` (version 1.4.1), we reprocessed the data with the latest calibration files available in the NuSTAR calibration database. Clean event files were generated using the `nupipeline` task, applying the standard filtering criteria. For source and background extraction, we used circular regions with radii of 60″ and 90″, respectively. The source region was centered at the position of the optical counterpart, whereas the background region was chosen away from the source. Spectra were extracted using the `nuproducts` task and rebinned to ensure a minimum of 20 counts per bin using the GRPPHA tool.

2.2.4. Suzaku

We used four *Suzaku* observations for our analysis, utilizing data from the X-ray Imaging Spectrometer (XIS) and the Hard X-ray Detector (HXD). The XIS consisted of four CCDs: XIS-0, XIS-2, and XIS-3 (front-illuminated), and XIS-1 (back-illuminated). Since XIS-2 was non-operational, only XIS-0, XIS-1, and XIS-3 were used. Standard data reduction was performed using FTOOLS v6.25 with the latest calibration files. Source and background spectra were extracted from a 250″ circular region centered on the source and away from the source, respectively. Response files were generated using XISRMFGEN and XISARFGEN. The XIS-0 and XIS-3 spectra (2–10 keV) were combined using ADDASCASPEC, while the XIS-1 spectrum (0.5−10 keV) was analyzed separately. The 1.6−2 keV range was excluded due to the known Si edge. All spectra were binned to a minimum of 20 counts per bin using GRPPHA.

For the HXD/PIN data, cleaned event files were processed with AEPIPELINE, and deadtime-corrected spectra were generated using HXDPINXBPI, incorporating both the non-X-ray background (Fukazawa et al. 2009) and simulated cosmic X-ray background (Gruber et al. 1999). HXD/PIN spectra in the 15−40 keV range were used for analysis.

3. Data analysis

3.1. Swift/XRT

We performed the spectral analysis using XSPEC version 12.13.1 (Arnaud 1996). The 0.5−10 keV *Swift*/XRT spectra were modeled with three components that are modified by absorption. We used BLACKBODY (ZBB), CUTOFFPL (ZCUT), and PEXRAV (Magdziarz et al. 1998) models for the soft X-ray emission, primary continuum emission with high-energy cutoff, and reprocessed emission, respectively. We employed two absorption components to account for both Galactic and intrinsic obscuration. Both absorption components were modeled with PHABS models. We also added a Gaussian line (GA) at ∼6.4 keV for the Fe K-line if present. In XSPEC terminology, the full model is PHABS*ZPHABS*(ZBB + ZCUT + PEXRAV + ZGA).

During the analysis, we fixed the high-energy cutoff $E_{\rm cut}$ at 200 keV, as it is expected to be higher than the *Swift*/XRT coverage. We tied the Γ, $E_{\rm cut}$, and the normalization of PEXRAV model to that of the ZCUT model. We fixed the inclination angle (i) at 30°, iron ($A_{\rm Fe}$), and metal abundances ($A_{\rm M}$) at solar value (i.e., 1). The only free parameter of the PEXRAV model is therefore the reflection fraction ($R_{\rm f}$).

For some observations we could not constrain the ZBB model parameters, and so fixed the blackbody temperature ($kT_{\rm BB}$) at 120 eV, which is the median for our sample. We obtained an upper limit of the BB flux from these observations. The Gaussian line width (LW) was fixed based on initial fits. The LW was set to 0.1, 0.05, or 0.01 keV for initial values in the ranges ∼0.07–0.12, 0.03–0.07, and 0.005–0.03 keV, respectively. We used Cash statistics for spectral fitting over the 0.5−8 keV XRT band and estimated 90% confidence intervals (1.6σ) using the ERROR command in XSPEC. All spectra yielded good fits (C/d.o.f. ∼ 1). The detailed result of the *Swift*/XRT analysis is available online through the CDS.

3.2. Broadband X-ray analysis

For the broadband X-ray analysis, we used *NuSTAR* and *Suzaku*/HXD-PIN for the hard X-ray band, and *Swift*/XRT, *Suzaku*/XIS, and *XMM-Newton*/EPIC-PN for the soft band. We applied the same spectral model as in the *Swift*/XRT analysis. A cross-normalization factor (C) was included to account for instrument differences. Unlike in the XRT analysis, we allowed $E_{\rm cut}$ in the ZCUT model to vary. The Γ, $E_{\rm cut}$, and normalization of PEXRAV were tied to ZCUT. The inclination (i), iron ($A_{\rm Fe}$), and metal abundances ($A_{\rm M}$) were fixed at 30°, 1, and 1, respectively. When the BLACKBODY parameters could not be constrained, we fixed $kT_{\rm BB}$ at 120 eV.

We used χ^2 statistics for spectral fitting and estimated 90% confidence intervals (1.6σ) using the ERROR command in XSPEC. Results of the broadband fits are detailed in Section 3.2. Figure 1 shows representative spectra of NGC 1566 in both type 1 and type 2 states in the left and right panels, respectively. The middle panels show residuals without SE components, while the bottom panels show residuals from the full model.

3.3. Eddington ratio and bolometric luminosity

Using *Swift*/UVOT and *Swift*/XRT observations, we studied the UV to X-ray SEDs using three component models: diskbb, blackbody, and cutoff power-law for disk, SE, and continuum emission, respectively. From the spectral modeling, we estimated the disk luminosity ($L_{\rm disk}$) in 10^{-7} − 0.5 keV, SE luminosity ($L_{\rm SE}$) in 0.001–10 keV, and continuum luminosity ($L_{\rm PL}$) in 0.1–500 keV. Then we calculated the bolometric luminosity as $L_{\rm bol} = L_{\rm disk} + L_{\rm SE} + L_{\rm PL}$. When we had calculated $L_{\rm bol}$, the Eddington ratio was estimated as $\lambda_{\rm Edd} = L_{\rm bol}/L_{\rm Edd}$, where $L_{\rm Edd} = 1.5 \times 10^{38} (M_{\rm BH}/M_{\odot})\,{\rm erg\,s^{-1}}$ is the Eddington luminosity. Our results are in good agreement with Gupta et al. (2024), who derived $\lambda_{\rm Edd}$-dependent bolometric correction factors (κ_{2-10}) from the SED analysis of unobscured AGNs in the BASS sample. The detailed SED fitting will be presented in a forthcoming publication.

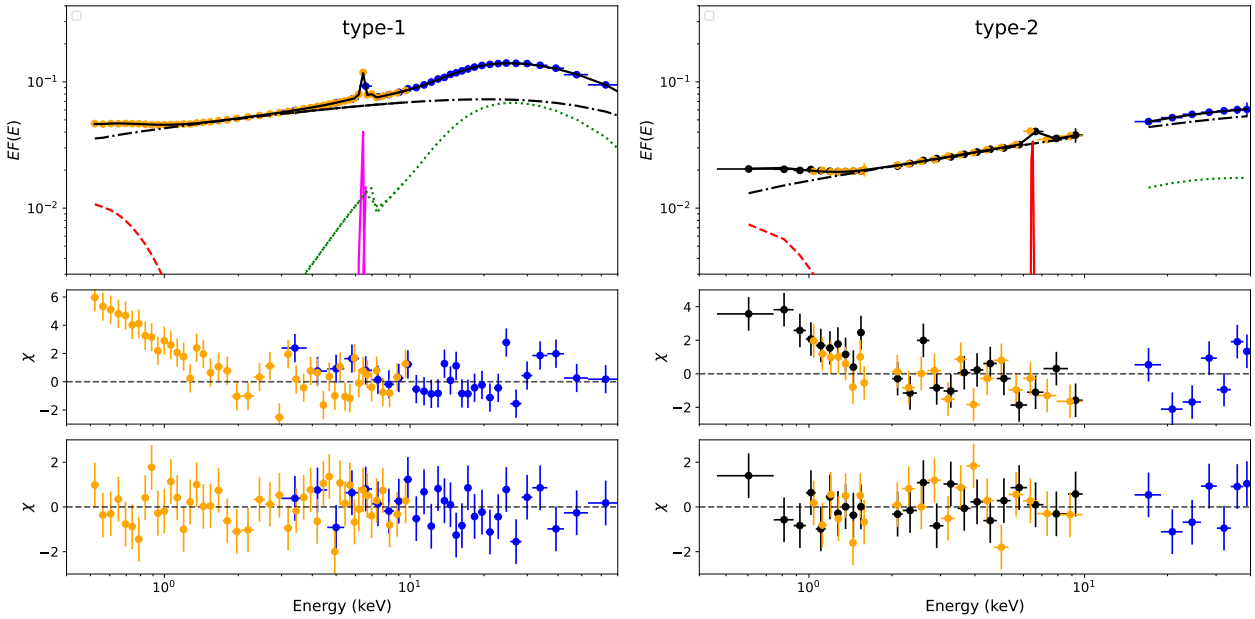

Fig. 1. Representative unfolded broadband X-ray spectra of NGC 1566 in type 1 and type 2 states (left and right panel, respectively). In the left panel, the orange and blue points represent the data from *XMM-Newton*/EPIC-PN and *NuSTAR*/FPMA observations, respectively. In the right panels, the black, orange, and blue points represent the *Suzaku*/XIS1, *Suzaku*/XIS0+XIS3, and *Suzaku*/HXD-PIN observations, respectively. The solid black, dot-dashed black, red dashed, solid magenta, and dotted green lines represent the total, continuum, soft excess, iron K-line, and reprocessed emission, respectively. The middle figures of each panel show the residual, while the data are fitted without the soft excess components. The bottom panels show the residuals for the full models.

3.4. Parameter estimation

We obtained several parameters from the spectral analysis, namely $kT_{\rm BB}$, Γ, $E_{\rm cut}$, and $R_{\rm f}$. We also calculated the SE flux ($F_{\rm SE}^{0.5-2}$), continuum flux ($F_{\rm PC}^{2-10}$), and reflection flux ($F_{\rm ref}^{10-40}$), using the BLACKBODY component in the 0.5–2 keV range, CUTOFFPL in 2–10 keV, and PEXRAV in 10–40 keV, respectively. We chose the 0.5–2 keV energy range to represent $F_{\rm SE}^{0.5-2}$ as BLACKBODY with $kT_{\rm BB} \sim 0.1-0.2$ keV is unlikely to contribute to the flux above 2 keV significantly. We represent the continuum emission in the 2–10 keV energy range, as this energy range has historically been used to present the continuum emission. As the reflection hump is generally observed to be most dominant in the ∼10–40 keV energy range, we used this energy range to represent $F_{\rm ref}^{10-40}$.

We defined the soft excess strength (Q) as the ratio of the SE to the continuum luminosity:

$$Q = L_{\rm SE}^{0.5-2}/L_{\rm PC}^{2-10}. \quad (1)$$

We also calculated the reflection strength as $R_{\rm S} = F_{\rm ref}^{10-40}/F_{\rm PC}^{2-10}$.

Following Jana et al. (2025), we marked spectral type 1–1.5 as type 1 and type 1.8–2 as type 2 in this work. Since simultaneous optical spectra are scarce, we assigned the optical state of each observation based on the nearest available optical spectral classification. Figure 2 displays the light curve of all five CSAGNs in different panels. The blue circles and orange diamonds mark the type 1 and type 2 states, respectively. The vertical lines in each panel represent the optical observations. The solid horizontal lines in each panel represents the median of transition Eddington ratio, $\log \lambda_{\rm Edd}^{\rm tr}$ at -2.01 ± 0.23 (from Jana et al. 2025). The dot-dashed horizontal lines represent the break-Eddington ratio in the V-shaped $\lambda_{\rm Edd} - \Gamma$ relation ($\log \lambda_{\rm Edd}^{\rm break} = -2.47 \pm 0.09$, see Section 4.3 for details).

We caution that some observations show type 2 state at high $\lambda_{\rm Edd}$, while some exhibit type 1 state at low $\lambda_{\rm Edd}$. This discrepancy may reflect the response time of the BLR to changes in the accretion rate. Moreover, the lack of simultaneous optical data for all X-ray observations may lead to misclassifications, especially during the state transitions.

3.5. Distribution of parameters

In our sample, $L_{\rm PC}^{2-10}$ was found to be in the range $\sim 10^{41}-10^{44}$ erg s^{-1} . The median of $\log L_{\rm PC}^{2-10}$ for type 1 and type 2 states was found to be 42.89 ± 0.03 and 42.35 ± 0.16, respectively. The SE spanned four orders of magnitude, in the range $\sim 10^{39-43}$ erg s^{-1}.

In several observations, only upper limits on the SE flux were available. For these, we performed 1000 Monte Carlo simulations by sampling the BLACKBODY normalization ($N_{\rm BB}$) uniformly between 0 and its upper limit, and computing the SE flux in each trial. The median was estimated using bootstrapping (see Ricci et al. 2018; Gupta et al. 2021, for details). The resulting median $\log L_{\rm SE}^{0.5-2}$ values are 41.80 ± 0.07 and 40.72 ± 0.20 in the type 1 and type 2 states, respectively.

Figure 3 shows the distribution of $kT_{\rm BB}$, which lies in the ∼80–160 eV range and is similar across states, with medians at 122.5 ± 1.4 eV and 120.0 ± 0.1 eV in type 1 and type 2, respectively. The photon index (Γ) is obtained in range of ∼1.5–2.1, with medians of 1.72 ± 0.01 and 1.69 ± 0.02 in the type 1 and type 2 states, respectively.

$\log \lambda_{\rm Edd}$ spans ∼−3.6 to −0.5 in our sample. The median of $\log \lambda_{\rm Edd}$ for the two AGN types is obtained at -1.63 ± 0.06 and -2.67 ± 0.05, respectively. In type 1 $\log Q$ peaks around ~ -0.75 to −1.25, while in type 2 it is more evenly spread from ~ -2.4 to −1.25. Median values of $\log Q$ are -1.10 ± 0.03 and -1.73 ± 0.07 in the type 1 and type 2 states, respectively. The median values of all parameters are listed in Table 2.

To investigate the correlation between the different parameters, we used Spearman rank correlation. The correlation index

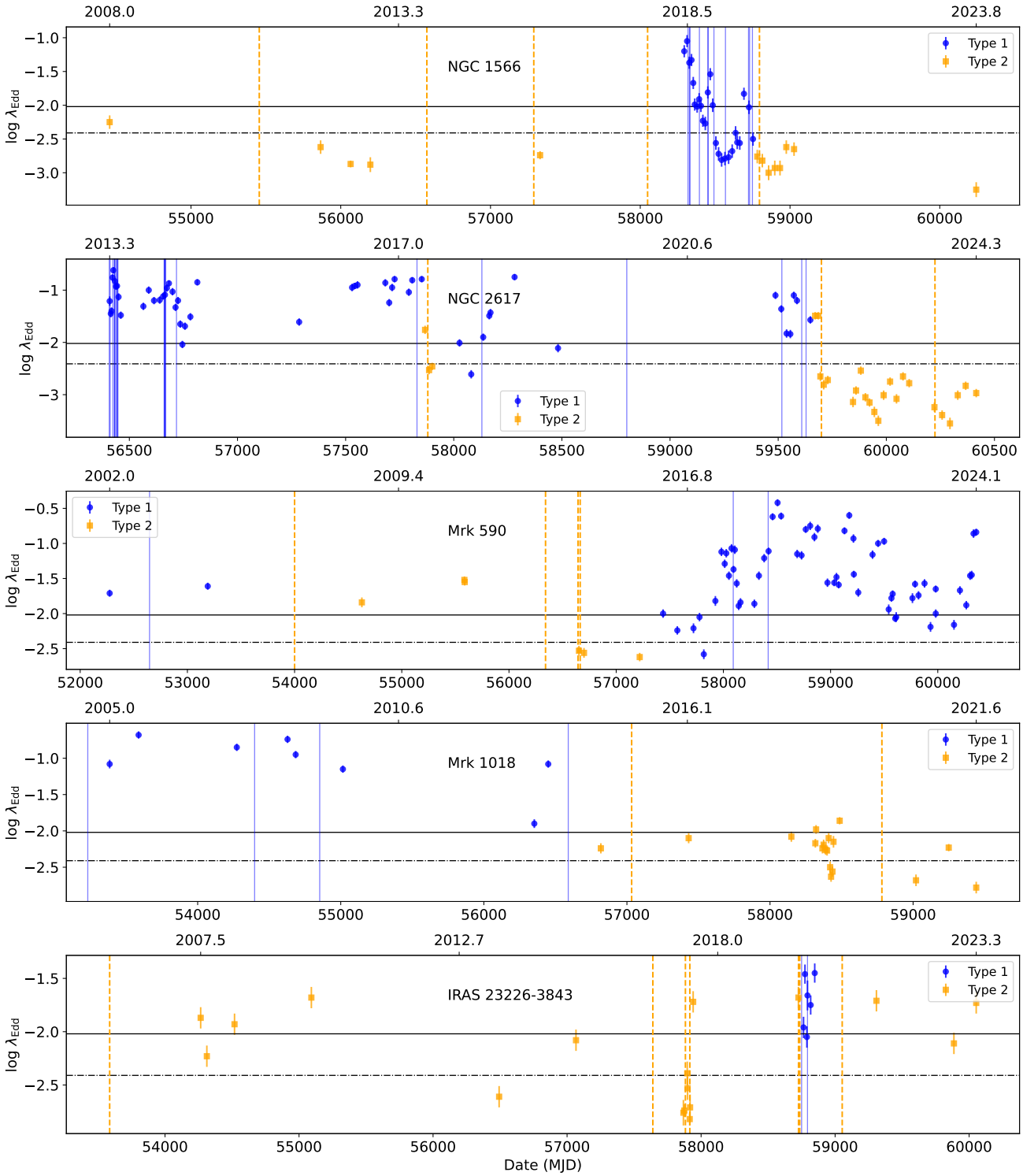

Fig. 2. Light curves of all five CSAGNs in different panels. The blue circles and orange diamonds mark the type 1 and type 2 states, respectively. The vertical lines in each panel represent the optical observations, where the solid blue and orange dot-dashed lines represent the type 1 and type 2 spectral states, respectively. The solid horizontal line in each panel represents the median of transition Eddington ratio $\log \lambda_{\rm Edd}^{\rm tr}$ at -2.01 ± 0.23 from Jana et al. (2025). The dot-dashed horizontal line represents the break-Eddington ratio ($\log \lambda_{\rm Edd}^{\rm break} = -2.47 \pm 0.098$.)

and p-values are listed in Table 3. To investigate the correlations between the various parameters, we performed linear fitting in logarithmic space. To properly account for censored data, we employed a bootstrap approach. For each upper limit a random value was drawn from a uniform distribution between zero and the upper limit, and for each measured value a random sample was drawn from a Gaussian distribution using the measurement uncertainty as the standard deviation. This procedure produced a simulated dataset, which was fitted using LINMIX (Kelly et al. 2009) to obtain the best fit. The procedure was repeated 1000 times, and the average parameters were adopted as the final best-fit values.

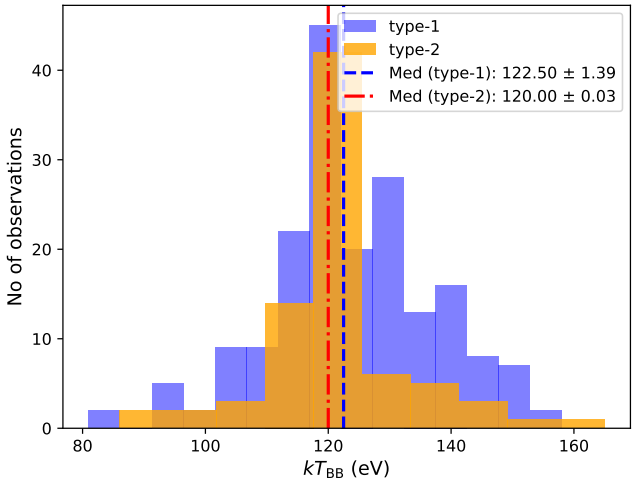

Fig. 3. Distribution of blackbody temperature (kT_{BB}). The blue dashed and red dot-dashed lines represent the median value for the type 1 and type 2 states, respectively.

Table 2. Median of the X-ray spectral fit parameters.

Parameters	Type 1	Type 2
$\log L_{PC}^{2-10}$ (erg s^{-1})	42.89 ± 0.03	42.35 ± 0.16
$\log L_{SE}^{0.5-2}$ (erg s^{-1})	41.80 ± 0.07	40.72 ± 0.20
kT_{BB} (eV)	122.5 ± 1.4	120.0 ± 0.1
Γ	1.72 ± 0.01	1.69 ± 0.02
$\log \lambda_{Edd}$	−1.63 ± 0.06	−2.67 ± 0.05
$\log Q$	−1.10 ± 0.03	−1.73 ± 0.07

Table 3. Spearman correlation analysis result.

Parameter 1	Parameter 1	ρ	p-value
$F_{SE}^{0.5-2}$	F_{PC}^{2-10}	0.93	$\ll 10^{-10}$
$L_{SE}^{0.5-2}$	L_{PC}^{2-10}	0.93	$\ll 10^{-10}$
Q	λ_{Edd}	0.86	$\ll 10^{-10}$
Q	R_S	–0.04	0.83

For visualization, we estimated binned medians using survival analysis with the SCIKIT-SURVIVAL package (Pölsterl 2020), which implements the Kaplan–Meier product limit (KMPL) estimator (Feigelson & Nelson 1985; Shimizu et al. 2017). This nonparametric method allows a robust estimation of median values in the presence of censored data. For each correlation, we computed KMPL-based medians in bins of the independent variable, ensuring at least 20 data points per bin.

4. Results and discussion

We studied five CSAGNs to investigate the origin of the SE and its relationship with primary continuum emission. As CSAGNs can show a wide range of λ_{Edd} on short timescales, we took advantage of CSAGNs to explore SE emission and its connection to the inner parts of the accretion flows in AGNs.

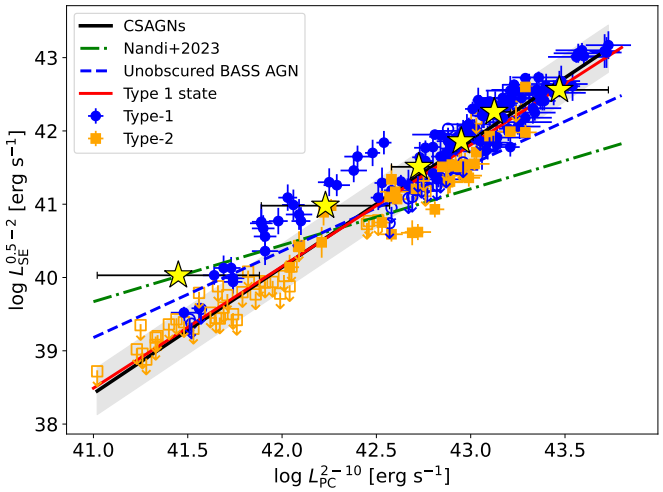

Fig. 4. Variation of the soft excess luminosity ($L_{SE}^{0.5-2}$) in 0.5–2 keV energy range as a function of continuum luminosity (L_{PC}^{2-10}) in 2–10 keV flux. The filled blue circles and orange squares represent the data from the type 1 and type 2 states, respectively. The open blue circles and orange squares represent the upper limit from the type 1 and type 2 state, respectively. The yellow stars represent the binned data points. The solid black line represents the linear best fit. The gray regions mark the 1σ scatter. The red solid line represents the linear best fit, considering only the type 1 state. The green dash-dotted and blue dashed lines represent the linear best fit for bare AGNs from Nandi et al. (2023) and unobscured BASS AGNs from Jana et al. (in prep.).

4.1. Soft excess temperature

We modeled the SE emission using a phenomenological blackbody component. From the spectral fits, we obtained the blackbody temperature (kT_{BB}) for each observation. To investigate whether kT_{BB} is related to the global properties of AGNs, we examined its dependence on several key parameters, namely L_{bol}, L_{PC}^{2-10}, $L_{SE}^{0.5-2}$, Q, λ_{Edd}, and M_{BH}. We found no statistically significant correlations between kT_{BB} and any of these AGN parameters. The soft excess temperature remains remarkably uniform across a wide range of AGN properties, consistent with previous studies (e.g., Gierliński & Done 2004; Petrucci et al. 2018).

4.2. Primary continuum and soft excess relation

We find a strong positive correlation between SE and PC emission ($p \ll 10^{-10}$). Figure 4 displays the variation of $L_{SE}^{0.5-2}$ as a function of L_{PC}^{2-10}. Using linear regression analysis in logarithmic space, we obtained

$$\log L_{SE,\,42}^{0.5-2} = (-1.77 \pm 0.08) + (1.71 \pm 0.17) \log L_{PC,\,42}^{2-10}, \quad (2)$$

with an intrinsic scatter of 0.22 dex. Here, $L_{SE,\,42}^{0.5-2} = (L_{SE}^{0.5-2}\,\mathrm{erg\,s^{-1}})/10^{42}$ and $L_{PC,\,42}^{2-10} = (L_{PC}^{2-10}\,\mathrm{erg\,s^{-1}})/10^{42}$. We also obtained similar results for $F_{SE}^{0.5-2} - F_{PC}^{2-10}$.

Previous studies have reported a strong positive correlation between SE and continuum flux in AGNs (e.g., Waddell & Gallo 2020; Nandi et al. 2023). Our fit yields a steep slope of ∼1.71, suggesting that SE emission increases more rapidly with PC emission than found in earlier works. For instance, Nandi et al. (2023) analyzed 20 unobscured AGNs and reported a shallower slope of 1.10 ± 0.04, using a power-law model over 0.5–10 keV. However, it is critical to note that their study used a power-law

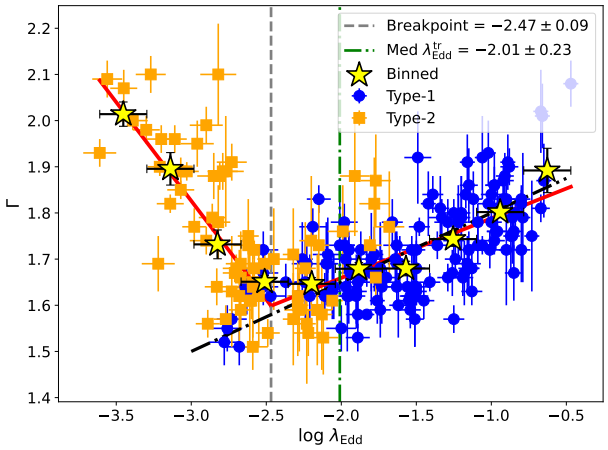

Fig. 5. Relation between Γ and $\lambda_{\rm Edd}$. The blue circles and orange squares represent the data from the type 1 and type 2 states, respectively. The yellow stars represent the binned data points. The red lines represent the linear best fit of the dataset with a break at $\log \lambda_{\rm Edd} = -2.47 \pm 0.09$. The break-point is marked by the vertical gray dashed line. The vertical green dash-dotted line represent the median of the transition Eddington ratio ($\lambda_{\rm Edd}^{\rm tr}$) for CSAGNs, which is $\log \lambda_{\rm Edd}^{\rm tr} = -2.01 \pm 0.23$. The $\lambda_{\rm Edd}^{\rm tr}$ is taken from Jana et al. (2025). The black dash-dotted line represents the $\Gamma - \lambda_{\rm Edd}$ relation of BASS AGNs, adopted from Trakhtenbrot et al. (2017).

model to fit the SE component and considered the 0.5–10 keV energy range for both SE and PC emission. We converted those to 0.5–2 keV for the SE and 2–10 keV for the PC emission, for direct comparison with our work. By doing this, we obtained a revised slope of 0.77 ± 0.04, which is significantly flatter than the value we derived from our own sample of CSAGNs.

A similar trend is found for unobscured AGNs in the BASS sample (Jana et al., in prep.), which also uses a BLACKBODY model for the SE. The slope for BASS AGNs is 0.73 ± 0.04, still flatter than our sample of CSAGNs. These consistently flatter slopes across different AGN samples, are possibly due to differences in their accretion properties, black hole masses, or spectral modeling approaches. Furthermore, both Nandi et al. (2023) and Jana et al. (in prep.) mainly focused on type 1 AGNs with $\lambda_{\rm Edd} > 0.01$, whereas our sample spans a broader range of $\lambda_{\rm Edd}$ (∼0.0003−0.3) and includes both type 1 and type 2 states.

To test the impact of AGN classification, we repeated our analysis using only CSAGNs in the type 1 state. The slope remains steep at 1.66 ± 0.21, which is consistent with the whole sample, and remains significantly steeper than the results of previous studies of type 1 AGNs. The strong SE-PC correlation across a large range of $\lambda_{\rm Edd}$ supports a common origin, possibly low-temperature Comptonization in a warm corona (e.g., Petrucci et al. 2018; Kubota & Done 2018).

4.3. $\Gamma - \lambda_{\rm Edd}$ relation and CS transitions

The $\Gamma - \lambda_{\rm Edd}$ relation provides important insights into AGN accretion and disk-corona coupling (Shemmer et al. 2006; Brightman et al. 2013; Yang et al. 2015; Trakhtenbrot et al. 2017, and references therein). Figure 5 shows this relation for our sample. A single-component linear fit of the form $\Gamma = A + B \log \lambda_{\rm Edd}$ fails to capture the observed trend. A two-component linear model with a break at $\log \lambda_{\rm Edd}^{\rm break} = -2.47 \pm 0.09$ significantly improves the fit, indicating a fundamental change in the accretion properties of AGNs at this $\lambda_{\rm Edd}$.

For $\lambda_{\rm Edd} > \lambda_{\rm Edd}^{\rm break}$ we found a positive correlation between Γ and $\lambda_{\rm Edd}$, with a slope of 0.13 ± 0.07, indicating that AGNs in this regime exhibit a softer X-ray spectrum at higher accretion rates. This trend is consistent with findings obtained by previous studies focused on nearby BASS AGNs (e.g., Trakhtenbrot et al. 2017), which also reported a similar positive Γ–$\lambda_{\rm Edd}$ relation with a slope of ∼0.15 for $\log \lambda_{\rm Edd} > -2.5$. In contrast, for AGNs with $\lambda_{\rm Edd} < \lambda_{\rm Edd}^{\rm break}$, we observed a negative correlation, with a slope of −0.44 ± 0.11. We analyzed the variation of individual CSAGNs in our sample, which revealed a range of $\lambda_{\rm Edd}^{\rm break}$ values, from 0.003 to 0.006 (see Appendix B). This variation in $\lambda_{\rm Edd}^{\rm break}$ suggests that the transition in the Γ–$\lambda_{\rm Edd}$ relation is a general feature in CSAGNs and occurs around $\log \lambda_{\rm Edd} \sim -2$ to −3.

Previous studies reported a possible V-shaped $\Gamma - \lambda_{\rm Edd}$ relation with breaks around $\log \lambda_{\rm Edd} \sim -2$ to −2.5 (Gu & Cao 2009; She et al. 2018; Diaz et al. 2023). Recently, Diaz et al. (2023) studied a sample of low-luminosity AGNs and found a similar break at $\log \lambda_{\rm Edd} \sim -2.39$, which closely matches our findings. She et al. (2018) also reported a break at $\log \lambda_{\rm Edd} \sim -2.5$ while studying a sample of nearby AGNs with *Chandra* observations. The break observed in the $\Gamma - \lambda_{\rm Edd}$ relation is consistent with a transition between two distinct accretion states, similar to the hard to soft spectral state transitions observed in BHXBs (e.g., Remillard & McClintock 2006; Gu & Cao 2009; Jana et al. 2022). This is in agreement with theoretical expectations and recent observations, which suggest that CSAGNs are undergoing state transitions, analogous to the hard to soft transitions in BHXBs (e.g., Noda & Done 2018; Ross et al. 2018; Ruan et al. 2019; Ai et al. 2020; Yan et al. 2020; Hagen et al. 2024; Kang et al. 2025). In agreement with this idea, using a sample of AGNs that includes the sources analyzed here, Jana et al. (2025) showed that the median of transition Eddington ratio ($\lambda_{\rm Edd}^{\rm tr}$; at which CSAGNs switch between type 1 and type 2 states) is $\log \lambda_{\rm Edd}^{\rm tr} = -2.01 \pm 0.23$, which is similar to $\log \lambda_{\rm Edd}^{\rm break} = -2.47 \pm 0.09$.

4.4. Relation between soft excess and Eddington ratio

To understand how the SE emission changes in the variable objects studied here, we studied the dependence of Q (Eq. (1)) on different AGN parameters. Several studies suggest that SE emission varies with AGN properties, hinting at a close connection between SE and the accretion process (e.g., Boissay et al. 2016; Noda & Done 2018; Ghosh et al. 2022; Mehdipour et al. 2023; Nandi et al. 2023; Chen et al. 2025). In some cases, particularly at low flux levels, SE emission has been observed to disappear completely, suggesting a strong connection between SE strength and the accretion process (e.g., Noda & Done 2018; Ghosh et al. 2022).

We studied the dependence of Q on $\lambda_{\rm Edd}$, a fundamental parameter thought to govern the physics of accretion in AGNs (e.g., Done et al. 2007; Ricci et al. 2018; Gupta et al. 2025). We find that as $\lambda_{\rm Edd}$ increases, the SE emission becomes significantly stronger. Figure 6 shows a strong positive correlation between Q and $\lambda_{\rm Edd}$ ($p \ll 10^{-10}$). The $Q - \lambda_{\rm Edd}$ relation is best described by a second-order polynomial fit,

$$\log Q = (-0.078 \pm 0.019)[\log \lambda_{\rm Edd}]^2 + (0.382 \pm 0.072) \log \lambda_{\rm Edd} - (0.339 \pm 0.088), \quad (3)$$

with an intrinsic scatter of 0.19 dex.

A positive correlation between Q and $\lambda_{\rm Edd}$ was originally reported by Boissay et al. (2016) for a sample of 102 hard X-ray selected Seyfert 1 galaxies, although with a very large scatter and

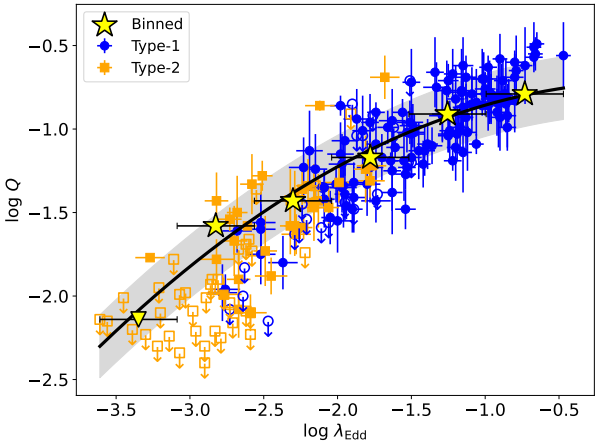

Fig. 6. Soft excess strength (Q) as a function of Eddington ratio ($\lambda_{\rm Edd}$). The filled blue circles and orange squares represent the data from type 1 and type 2 states, respectively, while the open blue circles and orange squares represent the upper limits from type 1 and type 2 state, respectively. The yellow stars represent the binned data points, while the yellow down triangle represents the upper limit. The black dashed line represents the best fit. The gray region marks the 1σ scatter.

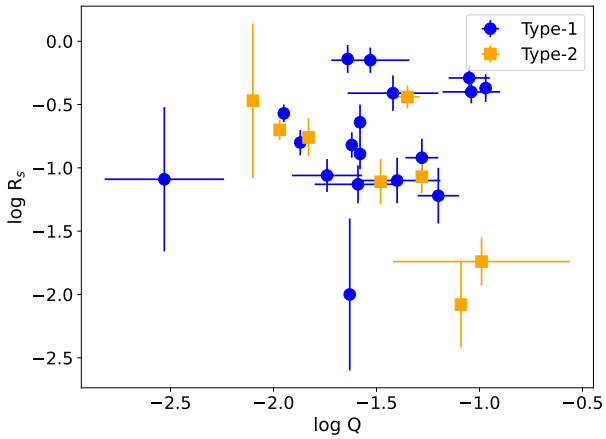

Fig. 7. Soft excess strength (Q) as a function of reflection strength ($R_{\rm S}$). The blue circles and orange squares represent the data from type 1 and type 2 states, respectively.

flatter slope. Similarly, Waddell & Gallo (2020) suggested the presence of this trend for broad-line Seyfert 1 (BLS1) galaxies, but found that the correlation weakens for narrow-line Seyfert 1 (NLS1) galaxies, which are typically high $\lambda_{\rm Edd}$ sources. Unlike these studies, our sample includes lower-luminosity AGNs, enabling us to probe SE behavior at $\lambda_{\rm Edd} < 0.01$. In this regime, Q declines sharply, and in many cases the soft excess is not detected, indicating that SE emission weakens or disappears at very low accretion rates. A similar behavior has also been observed in some AGNs where SE emission weakens at the low-accretion state (e.g., Noda & Done 2018; Hagen et al. 2024; Chen et al. 2025).

The $Q - \lambda_{\rm Edd}$ trend we find supports a scenario in which SE emission is closely linked to the inner accretion flow and corona. In both warm Comptonization and blurred reflection scenarios one could expect an enhanced SE at higher $\lambda_{\rm Edd}$ due to increased disk ionization and/or density. For more details, see Sect. 2.9 of the Language Guide. or more efficient disk-corona coupling. In the reflection scenario, at low $\lambda_{\rm Edd}$, the disk may recede and the corona may expand, reducing the reprocessing efficiency, and thus the SE emission (e.g., Reis & Miller 2013; Done et al. 2007; Wilkins et al. 2016). At high accretion rates, the disk would be more ionized, with an inner radius closer to the ISCO, resulting in stronger reflection. On the other hand, in the warm Comptonization scenario at low $\lambda_{\rm Edd}$, the warm corona may become inefficient or the inner accretion disk may transition to a radiatively inefficient flow, leading to the suppression or disappearance of the soft excess emission (e.g., Mehdipour et al. 2023; Layek et al. 2024). The disappearance or weakening of SE emission at very low $\lambda_{\rm Edd}$ suggests that at $\lambda_{\rm Edd} < 0.01$ the conditions required to produce SE are no longer sustained.

4.5. The relation between soft excess and Compton hump

To quantify the influence of the Compton hump, we parameterized it using the reflection strength ($R_{\rm S}$). Figure 7 illustrates the variation of $R_{\rm S}$ as a function of Q. We did not find any significant correlation between these two quantities, with a p-value of 0.83, suggesting that the reflection strength in CSAGNs is not strongly dependent on Q. If the SE originates primarily from blurred reflection, a positive correlation between Q and $R_{\rm S}$ is expected (e.g., Vasudevan et al. 2014; Boissay et al. 2016). However, our results do not support this scenario, which implies that SE and reflection arise from different physical processes. A study by Waddell & Gallo (2020) found a positive correlation between Q and the hard X-ray excess (similar to $R_{\rm S}$) in a sample of NLS1 galaxies, but no correlation in BLS1 galaxies. The authors suggested that in NLS1s, SE originates from reflection, whereas in BLS1s, alternative mechanisms such as warm Comptonization or ionized absorption may be responsible.

We note that the neutral reflection from the torus and BLR also could contribute to the Compton hump, along with the reflection from the disk. The reflection properties of our sample were extensively investigated in previous studies, which consistently report very weak or negligible reflection signatures (e.g., Parker et al. 2019; Jana et al. 2021; Ghosh et al. 2022; Tripathi & Dewangan 2022; Veronese et al. 2024). In many cases, the spectra can be adequately modeled without requiring any reflection component. Even if the torus or the BLR contributes to the Compton hump, the contribution is minimal, and the overall Compton hump flux (torus + ionized disk) remains weak. The combination of a strong SE and weak or absent Compton hump disfavors ionized reflection as the dominant origin of the SE.

4.6. Soft excess and photon index relation

We explored the relationship between Γ and Q for our sample and found a V-shaped $\Gamma - Q$ relation (Figure 8), similar to the relation between Γ and $\lambda_{\rm Edd}$. A Spearman correlation analysis yielded a correlation coefficient of -0.22 with $p = 0.33$ for $\log Q < -1.53$, and 0.71 with $p \ll 10^{-5}$ for $\log Q > -1.53$. Given the strong correlation between Q and $\lambda_{\rm Edd}$, the presence of this break is expected.

Boissay et al. (2016) found a positive correlation between Q and Γ. Their sample consisted of AGNs with $\log \lambda_{\rm Edd} > -2.2$, and therefore our findings for $\log Q > -1.53$ (corresponding to $\log \lambda_{\rm Edd} \sim -2.6$) are consistent with their results. Additionally, Boissay et al. (2016) predicted a weak negative correlation between Γ and Q under an ionized reflection scenario using simulations carried out with the `relxillp_ion` model. As the result of this study is consistent with the finding of

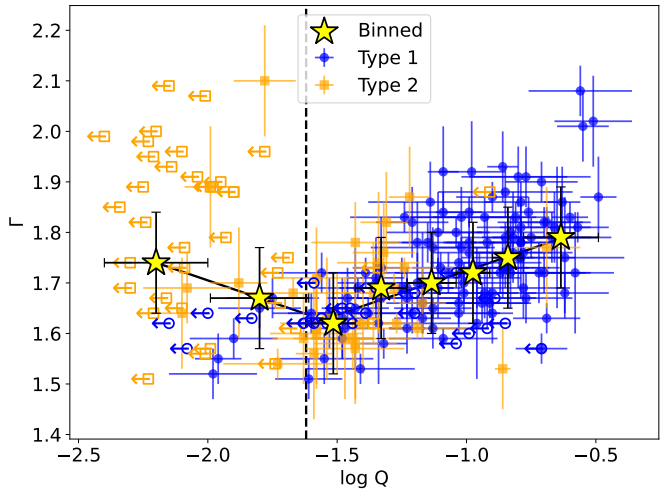

Fig. 8. Relation between photon index (Γ) and the soft excess strength (Q) is shown. The blue circles and orange squares represent the data from type 1 and type 2 states, respectively. The open blue circles and orange squares represent the upper limit from type 1 and type 2 states, respectively. The yellow stars represent the binned data points. The black solid lines represent the linear best fit of the dataset with a break at $\log Q = -1.62 \pm 0.12$, which corresponds to $\log \lambda_{\rm Edd} = -2.60 \pm 0.14$. The break-point is marked by the vertical black dashed line.

Boissay et al. (2016), our findings are inconsistent with the ionized reflection scenario for $\log \lambda_{\rm Edd} > -2.6$. For $\log Q < -1.53$ (i.e., $\log \lambda_{\rm Edd} < -2.2$), no correlation is observed between Γ and Q, as we mostly observed an upper limit of Q. This suggests that, in this accretion regime, the warm corona may not be linked to the hot corona or it becomes extremely weak.

4.7. The origin of the soft excess

The soft excess remains a long-standing puzzle four decades after its discovery (Arnaud et al. 1985; Singh et al. 1985). Understanding the physical mechanisms responsible for the SE is crucial, as it directly impacts our understanding of accretion processes in AGNs. In the ionized reflection scenario, SE arises from reflection off an ionized AD close to the SMBH. Several studies, including those of Vasudevan et al. (2014) and Boissay et al. (2016), have predicted specific correlations between spectral parameters within this framework. While a positive correlation between $R_{\rm S}$ and Q, as well as a negative correlation between Γ and Q, are expected, we find no such trends (see Figs. 8 and 7). Moreover, our broadband spectra show weak or absent Compton humps, a key signature of reflection-dominated spectra (Ross & Fabian 2005; Walton et al. 2013). The absence of strong reprocessed emission across a wide range of $\lambda_{\rm Edd}$ further weakens the case for ionized reflection as the primary SE mechanism. This aligns with the findings of previous studies, which indicate that while ionized reflection can contribute to the SE in certain AGNs, it is unlikely to be the main mechanism producing this component (Gallo et al. 2019; Nandi et al. 2023).

In contrast, our results show a tight correlation between SE and continuum flux (see Fig. 4) across a wide range of $\lambda_{\rm Edd}$, favoring warm Comptonization. The tight $Q - \lambda_{\rm Edd}$ relation (see Fig. 5) implies that SE emission closely tracks accretion activity, consistent with models where UV disk photons are up-scattered in a warm, optically thick corona (Crummy et al. 2006; Done et al. 2012; Kubota & Done 2018; Middei et al. 2020). Recently, Palit et al. (2024) suggested that the warm corona size increases with $\lambda_{\rm Edd}$, enhancing SE emission (see also Chen et al. 2025), which is consistent with our findings.

Our study aligns with recent studies of CSAGNs, which suggest that warm Comptonization is the most likely origin for the SE (Jana et al. 2021; Tripathi & Dewangan 2022; Giustini et al. 2017; Veronese et al. 2024). For Mrk 590, Laha et al. (2022) found that both warm Comptonization and ionized reflection could fit the data. However, our analysis favors warm Comptonization as the leading explanation for SE in our sample. While ionized reflection can become significant in highly accreting AGNs ($\lambda_{\rm Edd} \sim 1$), this regime is beyond the scope of our study and will be explored in future works. Our results add to the growing consensus that warm Comptonization is a key mechanism shaping the soft X-ray excess in AGNs, especially in systems with moderate to low accretion rates ($\lambda_{\rm Edd} = 0.001-0.3$).

4.8. SE and CS transitions

The SE is believed to play a central role in regulating the ionization state of the BLR, with changes in its flux capable of substantially modifying the ionizing photon budget (Noda & Done 2018). Recent studies have shown that during CS transitions, the SE flux often varies more dramatically than the PC emission, suggesting a strong connection between SE variability and changes in AGN state (e.g., Noda & Done 2018; Mehdipour et al. 2022a). For our sample, we find that the median SE and PC luminosities in the type 1 state are $\sim 6.3 \times 10^{41}$ erg s^{-1} and $\sim 7.8 \times 10^{42}$ erg s^{-1}, respectively. In contrast, during the type 2 state, the corresponding median values drop to $\sim 5.2 \times 10^{40}$ erg s^{-1} and $\sim 2.2 \times 10^{42}$ erg s^{-1}. This corresponds to a factor of ∼12 change in the SE and a factor of ∼3.5 in the PC between the two states, further indicating that the SE exhibits stronger variability across CS transitions. Except for IRAS 23226–3843, the median SE luminosity changes more drastically than the PC luminosity between spectral states for all sources in our sample. This trend is consistent with the broader picture in which a decline in accretion rate reduces the extreme ultraviolet continuum, leading to fewer ionizing photons and, consequently, weaker or absent BELs (Noda & Done 2018; Ruan et al. 2019). Our finding is consistent with the previous studies of CSAGNs. For instance, in NGC 1566, the SE and PC increased by factors of ∼200 and ∼30, respectively, as the source transitioned from a type 2 to a type 1 state (Tripathi & Dewangan 2022). A similar trend has been observed in Mrk 1018, where the SE exhibited stronger variability than the PC across spectral transitions (Noda & Done 2018; Saha et al. 2025).

This trend is not restricted to a few rare CSAGNs, but is observed in the general AGN population. A few studies showed a sharp decline in the fraction of broad-line AGNs below $\lambda_{\rm Edd} \sim 0.01-0.02$ (Trump et al. 2011; Mitchell et al. 2023; Hagen et al. 2024; Kang et al. 2025), which coincides with the transition Eddington ratio for CSAGNs. Additionally, we find that the median Q, is ∼0.08 in the type 1 state and ∼0.02 in the type 2 state. This result is consistent with the interpretation that the SE diminishes more rapidly than the PC as AGNs transition to type 2 states. The strong dependence of both Q and SE luminosity on spectral state suggests that the SE is intrinsically connected to CS transitions (Noda & Done 2018). Table 4 shows how the median values of different parameters change between the type 1 and type 2 states.

Table 4. Factor of change in the median value of fluxes and soft excess strength between type 1 & type 2 states.

Source	f_{SE}	f_{PC}	f_Q
NGC 1566	51	4	17
NGC 2617	295	34	21
Mrk 590	35	7	8
Mrk 1018	48	16	7
IRAS 23226–3843	2	2	1.4

Notes. $f_{SE} = L^{0.5-2}_{SE,\ type\ 1}/L^{0.5-2}_{SE,\ type\ 2}$; $f_{PC} = L^{2-10}_{PC,\ type\ 1}/L^{2-10}_{PC,\ type\ 2}$; $f_Q = Q_{type\ 1}/Q_{type\ 2}$.

5. Summary and conclusions

We investigated the X-ray properties of a sample of five CSAGNs to understand the nature of their inner accretion flow, soft excess emission, and their connection to CS transitions. We used a total 42 *XMM-Newton*, 4 *Suzaku*, 22 *NuSTAR*, and 1021 *Swift*/XRT observations for our study. Our sample spans three orders of magnitude in Eddington ratios ($\lambda_{Edd} \sim 0.0003-0.3$) and covers both type 1 and type 2 states. Based on the broadband X-ray spectral study, we retrieved several accretion parameters, namely photon index, blackbody temperature, soft excess strength, soft excess, and primary continuum luminosity. On the basis of multiple correlations, our findings suggest that SE emission originates from a warm corona across a broad range of accretion rates. In the following, we summarize our key findings:

1. We find that SE and PC emission are tightly correlated, with an intrinsic scatter of 0.22 dex (1σ) over four orders of magnitude in luminosity (Fig. 4). The soft excess luminosities cover a wider range than primary continuum luminosities, indicating that the SE is more variable than the continuum emission.
2. The SE emission in CSAGNs varies more rapidly than in AGNs that do not undergo CS transitions. The steeper slope in the SE-PC relation for CSAGNs suggests that these objects experience more pronounced spectral variations, possibly driven by rapid changes in the accretion rate. We also found that the SE emission changes more compared to the PC emission during the CS transitions, suggesting that the SE is intrinsically connected to the optical state change.
3. We observed a very clear V-shaped $\Gamma - \lambda_{Edd}$ relation with a break at $\log \lambda_{Edd} = -2.47 \pm 0.09$ (Fig. 5). This break is consistent with λ^{tr}_{Edd} for changing-state transitions, which is generally observed at $\lambda^{tr}_{Edd} \sim 0.005-0.015$.
4. The soft excess strength correlates positively with λ_{Edd} (Fig. 6), indicating that SE emission increases significantly in high-accretion states. This suggests a close connection between SE and the inner accretion disk.
5. We find no correlation between Q and the reflection strength (Fig. 7); this suggests that SE emission is not dominated by blurred reflection.
6. At high accretion rates ($\lambda_{Edd} > 0.001$), Q and Γ exhibit a positive correlation (Fig. 8).

Overall, from our sample, we find that the warm Comptonization scenario is the most likely origin of the SE, at least in the range of λ_{Edd} probed here ($\lambda_{Edd} \sim 0.003-0.3$). CSAGNs offer crucial insight into the structure and evolution of the inner accretion flow in SMBHs. Our results indicate that SE emission is closely linked to the continuum and is likely dominated by warm Comptonization. This warm coronal emission appears tightly connected to the accretion disk, which radiates primarily in the UV/optical. In a forthcoming study, we will present the UV/optical to X-ray SED to further explore this connection.

Future work will extend the analysis to higher λ_{Edd} AGNs (Kallova et al., in prep.; Kumari et al., in prep.) to examine warm Comptonization under different accretion regimes. We find that SE varies more rapidly than the PC during state transitions. Follow-up studies will explore the connection between SE and BELs to understand the physical drivers of BELs using multiwavelength data. To deepen our understanding of SE and its link to the primary X-ray continuum, future studies with larger AGN samples and high-resolution X-ray spectroscopy will be essential. Missions such as *XPOSAT* (Paul 2022; Vatedka et al. 2025) and *NewAthena* (Cruise et al. 2025) will help constrain the physical mechanisms behind SE. Additionally, proposed observatories such as *AXIS* (Reynolds et al. 2023) will be critical for building a comprehensive model of AGN accretion physics and X-ray emission evolution across AGN populations.

Data availability

All the data used in the paper are publicly available. The data are available at the CDS via https://cdsarc.cds.unistra.fr/viz-bin/cat/J/A+A/707/A213

Acknowledgements. We acknowledge support from ANID grants FONDECYT Postdoctoral fellowship 3230303 (AJ) and 3230310 (YD), ANID-Chile BASAL CATA FB210003 (FEB), FONDECYT Regular 1241005 (FEB), and the Millennium Science Initiative, AIM23-0001 (FEB). C.R.acknowledges support from SNSF Consolidator grant F01–13252, Fondecyt Regular grant 1230345, ANID BASAL project FB210003 and the China-Chile joint research fund. A.T. acknowledges financial support from the Bando Ricerca Fondamentale INAF 2022 Large Grant "Toward an holistic view of the Titans: multiband observations of $z > 6$ QSOs powered by greedy supermassive black holes". B.T. acknowledges support from the European Research Council (ERC) under the European Union's Horizon 2020 research and innovation program (grant agreement number 950533). This research was supported by the Excellence Cluster ORIGINS which is funded by the Deutsche Forschungsgemeinschaft (DFG, German Research Foundation) under Germany's Excellence Strategy – EXC 2094 – 390783311. B.T. also acknowledges the hospitality of the Instituto de Estudios Astrofísicos at Universidad Diego Portales, the Instituto de Astrofísica at Pontificia Universidad Católica de Chile, and the Institut d'Astrophysique de Paris, where parts of this study have been carried out. MJT acknowledges support from UKRI ST/X001075/1. M.K. acknowledges support from NASA through ADAP award 80NSSC22K1126. KKG acknowledges financial support from the Belgian Federal Science Policy Office (BELSPO) in the framework of the PRODEX Programme of the European Space Agency. HKC acknowledges supports the grant NSTC 113-2112-M-007-020. D.I. acknowledges funding provided by the University of Belgrade, Faculty of Mathematics (the contract 451-03-136/2025-03/200104) through the grants by the Ministry of Science, Technological Development and Innovation of the Republic of Serbia. E.S. acknowledges the support of the Alexander von Humboldt Foundation. This research has made use of data and/or software provided by the High Energy Astrophysics Science Archive Research Center (HEASARC), which is a service of the Astrophysics Science Division at NASA/GSFC and the High Energy Astrophysics Division of the Smithsonian Astrophysical Observatory. This work has made use of data obtained from the *NuSTAR* mission, a project led by Caltech, funded by NASA and managed by NASA/JPL, and has utilized the NuSTARDAS software package, jointly developed by the ASDC, Italy and Caltech, USA. This research has made use of observations obtained with *XMM–Newton*, an ESA science mission with instruments and contributions directly funded by ESA Member States and NASA. This work made use of XRT data supplied by the UK Swift Science Data Centre at the University of Leicester, UK. This work has made use of data obtained from *Suzaku*, a collaborative mission between the space agencies of Japan (JAXA) and the USA (NASA).

References

Ai, Y., Dou, L., Yang, C., et al. 2020, ApJ, 890, L29
Arnaud, K. A. 1996, ASP Conf. Ser., 101, 17
Arnaud, K. A., Branduardi-Raymont, G., Culhane, J. L., et al. 1985, MNRAS, 217, 105
Beuchert, T., Markowitz, A. G., Dauser, T., et al. 2017, A&A, 603, A50

Boissay, R., Ricci, C., & Paltani, S. 2016, A&A, 588, A70
Brightman, M., Silverman, J. D., Mainieri, V., et al. 2013, MNRAS, 433, 2485
Burrows, D. N., Hill, J. E., Nousek, J. A., et al. 2005, Space Sci. Rev., 120, 165
Chakrabarti, S., & Titarchuk, L. G. 1995, ApJ, 455, 623
Chen, S.-J., Wang, J.-X., Kang, J.-L., et al. 2025, ApJ, 980, 23
Chen, S.-J., Buchner, J., Liu, T., et al. 2025, A&A, 701, A144
Cohen, R. D., Rudy, R. J., Puetter, R. C., Ake, T. B., & Foltz, C. B. 1986, ApJ, 311, 135
Cruise, M., Guainazzi, M., Aird, J., et al. 2025, Nat. Astron., 9, 36
Crummy, J., Fabian, A. C., Gallo, L., & Ross, R. R. 2006, MNRAS, 365, 1067
Dauser, T., Garcia, J., Parker, M. L., Fabian, A. C., & Wilms, J. 2014, MNRAS, 444, L100
Dauser, T., García, J., Walton, D. J., et al. 2016, A&A, 590, A76
Denney, K. D., De Rosa, G., Croxall, K., et al. 2014, ApJ, 796, 134
Diaz, Y., Hernàndez-García, L., Arévalo, P., et al. 2023, A&A, 669, A114
Ding, Y., Garcıa, J. A., Kallman, T. R., et al. 2024, ApJ, 974, 280
Done, C., Gierliński, M., & Kubota, A. 2007, A&ARv, 15, 1
Done, C., Davis, S. W., Jin, C., Blaes, O., & Ward, M. 2012, MNRAS, 420, 1848
Edelson, R., Gelbord, J., Cackett, E., et al. 2017, ApJ, 840, 41
Emmanoulopoulos, D., Papadakis, I. E., McHardy, I. M., et al. 2012, MNRAS, 424, 1327
Esin, A. A., McClintock, J. E., & Narayan, R. 1997, ApJ, 489, 865
Evans, P. A., Beardmore, A. P., Page, K. L., et al. 2009, MNRAS, 397, 1177
Feigelson, E. D., & Nelson, P. I. 1985, ApJ, 293, 192
Fender, R., & Belloni, T. 2004, ARA&A, 42, 317
Feng, H.-C., Liu, H. T., Bai, J. M., et al. 2021, ApJ, 912, 92
Frank, J., King, A., & Raine, D. J. 2002, Accretion Power in Astrophysics (Third Edition (Cambridge University Press))
Fukazawa, Y., Mizuno, T., Watanabe, S., et al. 2009, PASJ, 61, S17
Gallo, L. C., Gonzalez, A. G., Waddell, S. G. H., et al. 2019, MNRAS, 484, 4287
García, J., & Kallman, T. R. 2010, ApJ, 718, 695
García, J. A., Kara, E., Walton, D., et al. 2019, ApJ, 871, 88
Ghosh, R., Laha, S., Deshmukh, K., et al. 2022, ApJ, 937, 31
Gierliński, M., & Done, C. 2004, MNRAS, 349, L7
Giustini, M., Costantini, E., De Marco, B., et al. 2017, A&A, 597, A66
Gruber, D. E., Matteson, J. L., Peterson, L. E., & Jung, G. V. 1999, ApJ, 520, 124
Gu, M., & Cao, X. 2009, MNRAS, 399, 349
Gupta, K. K., Ricci, C., Tortosa, A., et al. 2021, MNRAS, 504, 428
Gupta, K. K., Ricci, C., Temple, M. J., et al. 2024, A&A, 691, A203
Gupta, K. K., Ricci, C., Tortosa, A., et al. 2025, ApJ, 990, 86
Haardt, F., & Maraschi, L. 1991, ApJ, 380, L51
Hagen, S., Done, C., Silverman, J. D., et al. 2024, MNRAS, 534, 2803
Harrison, F. A., Craig, W. W., Christensen, F. E., et al. 2013, ApJ, 770, 103
Jana, A., Kumari, N., Nandi, P., et al. 2021, MNRAS, 507, 687
Jana, A., Ricci, C., Naik, S., et al. 2022, MNRAS, 512, 5942
Jana, A., Ricci, C., Temple, M. J., et al. 2025, A&A, 693, A35
Jansen, F., Lumb, D., Altieri, B., et al. 2001, A&A, 365, L1
Kang, J.-L., Done, C., Hagen, S., et al. 2025, MNRAS, 538, 121
Kawamuro, T., Ueda, Y., Tazaki, F., & Terashima, Y. 2013, ApJ, 770, 157
Kelly, B. C., Bechtold, J., & Siemiginowska, A. 2009, ApJ, 698, 895
Kollatschny, W., Grupe, D., Parker, M. L., et al. 2020, A&A, 638, A91
Kollatschny, W., Grupe, D., Parker, M. L., et al. 2023, A&A, 670, A103
Koratkar, A., Deustua, S. E., Heckman, T., et al. 1995, ApJ, 440, 132
Koss, M. J., Ricci, C., Trakhtenbrot, B., et al. 2022a, ApJS, 261, 2
Koss, M. J., Trakhtenbrot, B., Ricci, C., et al. 2022b, ApJS, 261, 6
Koyama, K., Tsunemi, H., Dotani, T., et al. 2007, PASJ, 59, 23
Krolik, J. H. 1999, Active Galactic Nuclei: From the Central Black Hole to the Galactic Environment (Princeton University Press)
Kubota, A., & Done, C. 2018, MNRAS, 480, 1247
Laha, S., Meyer, E., Roychowdhury, A., et al. 2022, ApJ, 931, 5
Lawther, D., Vestergaard, M., Raimundo, S., et al. 2023, MNRAS, 519, 3903
Layek, N., Nandi, P., Naik, S., et al. 2024, MNRAS, 528, 5269
Lu, K.-X., Li, Y.-R., Wu, Q., et al. 2025, ApJS, 276, 51
Lyu, B., Yan, Z., Yu, W., & Wu, Q. 2021, MNRAS, 506, 4188
Maccarone, T. J. 2003, A&A, 409, 697
MacLeod, C. L., Ross, N. P., Lawrence, A., et al. 2016, MNRAS, 457, 389
Magdziarz, P., Blaes, O. M., Zdziarski, A. A., Johnson, W. N., & Smith, D. A. 1998, MNRAS, 301, 179
Malkan, M. A., & Sargent, W. L. W. 1982, ApJ, 254, 22
McElroy, R. E., Husemann, B., Croom, S. M., et al. 2016, A&A, 593, L8
McHardy, I. M., Koerding, E., Knigge, C., Uttley, P., & Fender, R. P. 2006, Nature, 444, 730
Mehdipour, M., Kriss, G. A., Brenneman, L. W., et al. 2022a, ApJ, 925, 84
Mehdipour, M., Kriss, G. A., Costantini, E., et al. 2022b, ApJ, 934, L24
Mehdipour, M., Kriss, G. A., Kaastra, J. S., Costantini, E., & Mao, J. 2023, ApJ, 952, L5
Merloni, A., Heinz, S., & di Matteo, T. 2003, MNRAS, 345, 1057
Merloni, A., Dwelly, T., Salvato, M., et al. 2015, MNRAS, 452, 69
Middei, R., Petrucci, P. O., Bianchi, S., et al. 2020, A&A, 640, A99
Mitchell, J. A. J., Done, C., Ward, M. J., et al. 2023, MNRAS, 524, 1796
Nandi, P., Chatterjee, A., Jana, A., et al. 2023, ApJS, 269, 15
Netzer, H. 2013, The Physics and Evolution of Active Galactic Nuclei (Cambridge University Press)
Noda, H., & Done, C. 2018, MNRAS, 480, 3898
Ochmann, M. W., Kollatschny, W., & Zetzl, M. 2020, Contrib. Astron. Obs. Skalnate Pleso, 50, 318
Ochmann, M. W., Kollatschny, W., Probst, M. A., et al. 2024, A&A, 686, A17
Oh, K., Koss, M. J., Ueda, Y., et al. 2022, ApJS, 261, 4
Oknyansky, V. L., Gaskell, C. M., Huseynov, N. A., et al. 2017, MNRAS, 467, 1496
Oknyansky, V. L., Winkler, H., Tsygankov, S. S., et al. 2019, MNRAS, 483, 558
Oknyansky, V. L., Tsygankov, S. S., Dodin, A. S., et al. 2023, ATel, 16324, 1
Palit, B., Różańska, A., Petrucci, P. O., et al. 2024, A&A, 690, A308
Palit, B., Śniegowska, M., Markowitz, A., et al. 2025, MNRAS, 540, L14
Panda, S., & Śniegowska, M. 2024, ApJS, 272, 13
Parker, M. L., Schartel, N., Grupe, D., et al. 2019, MNRAS, 483, L88
Paul, B. 2022, in 44th COSPAR Scientific Assembly. Held 16–24 July, 44, 1853
Peca, A., Koss, M. J., Oh, K., et al. 2025, ApJ, 990, 3
Petrucci, P. O., Paltani, S., Malzac, J., et al. 2013, A&A, 549, A73
Petrucci, P. O., Ursini, F., De Rosa, A., et al. 2018, A&A, 611, A59
Pölsterl, S. 2020, J. Mach. Learn. Res., 21, 1
Rees, M. J. 1988, Nature, 333, 523
Reis, R. C., & Miller, J. M. 2013, ApJ, 769, L7
Remillard, R. A., & McClintock, J. E. 2006, ARA&A, 44, 49
Reynolds, C. S., Kara, E. A., Mushotzky, R. F., et al. 2023, SPIE Conf. Ser., 12678, 126781E
Ricci, C., & Trakhtenbrot, B. 2023, Nat. Astron., 7, 1282
Ricci, C., Trakhtenbrot, B., Koss, M. J., et al. 2017, ApJS, 233, 17
Ricci, C., Ho, L. C., Fabian, A. C., et al. 2018, MNRAS, 480, 1819
Ricci, C., Kara, E., Loewenstein, M., et al. 2020, ApJ, 898, L1
Ricci, C., Loewenstein, M., Kara, E., et al. 2021, ApJS, 255, 7
Risaliti, G., Elvis, M., Fabbiano, G., Baldi, A., & Zezas, A. 2005, ApJ, 623, L93
Risaliti, G., Salvati, M., Elvis, M., et al. 2009, MNRAS, 393, L1
Rivers, E., Markowitz, A., Duro, R., & Rothschild, R. 2012, ApJ, 759, 63
Ross, R. R., & Fabian, A. C. 2005, MNRAS, 358, 211
Ross, N. P., Ford, K. E. S., Graham, M., et al. 2018, MNRAS, 480, 4468
Ruan, J. J., Anderson, S. F., Eracleous, M., et al. 2019, ApJ, 883, 76
Saha, T., Krumpe, M., Markowitz, A., et al. 2025, A&A, 699, A205
Shakura, N. I., & Sunyaev, R. A. 1973, A&A, 500, 33
Shappee, B. J., Prieto, J. L., Grupe, D., et al. 2014, ApJ, 788, 48
She, R., Ho, L. C., Feng, H., & Cui, C. 2018, ApJ, 859, 152
Shemmer, O., Brandt, W. N., Netzer, H., Maiolino, R., & Kaspi, S. 2006, ApJ, 646, L29
Sheng, Z., Wang, T., Jiang, N., et al. 2017, ApJ, 846, L7
Shimizu, T. T., Mushotzky, R. F., Meléndez, M., et al. 2017, MNRAS, 466, 3161
Sikora, M., Stawarz, Ł., & Lasota, J.-P. 2007, ApJ, 658, 815
Singh, K. P., Garmire, G. P., & Nousek, J. 1985, ApJ, 297, 633
Sobolewska, M. A., Siemiginowska, A., & Gierliński, M. 2011, MNRAS, 413, 2259
Stern, D., McKernan, B., Graham, M. J., et al. 2018, ApJ, 864, 27
Sunyaev, R. A., & Titarchuk, L. G. 1980, A&A, 500, 167
Svoboda, J., Guainazzi, M., & Merloni, A. 2017, A&A, 603, A127
Takahashi, T., Abe, K., Endo, M., et al. 2007, PASJ, 59, 35
Temple, M. J., Ricci, C., Koss, M. J., et al. 2023, MNRAS, 518, 2938
Trakhtenbrot, B., Ricci, C., Koss, M. J., et al. 2017, MNRAS, 470, 800
Trakhtenbrot, B., Arcavi, I., MacLeod, C. L., et al. 2019, ApJ, 883, 94
Tripathi, P., & Dewangan, G. C. 2022, ApJ, 930, 117
Trump, J. R., Impey, C. D., Kelly, B. C., et al. 2011, ApJ, 733, 60
Vasudevan, R. V., & Fabian, A. C. 2007, MNRAS, 381, 1235
Vasudevan, R. V., Mushotzky, R. F., Reynolds, C. S., et al. 2014, ApJ, 785, 30
Vatedka, R., Tyagi, A., Vadodariya, K., et al. 2025, J. Astron. Telesc. Instrum. Syst., 11, 035001
Veronese, S., Vignali, C., Severgnini, P., Matzeu, G. A., & Cignoni, M. 2024, A&A, 683, A131
Waddell, S. G. H., & Gallo, L. C. 2020, MNRAS, 498, 5207
Walton, D. J., Nardini, E., Fabian, A. C., Gallo, L. C., & Reis, R. C. 2013, MNRAS, 428, 2901
Wilkins, D. R., Cackett, E. M., Fabian, A. C., & Reynolds, C. S. 2016, MNRAS, 458, 200
Xiang, X., Ballantyne, D. R., Bianchi, S., et al. 2022, MNRAS, 515, 353
Xu, D. W., Komossa, S., Grupe, D., et al. 2024, Universe, 10, 61
Yan, Z., Xie, F.-G., & Zhang, W. 2020, ApJ, 889, L18
Yang, Q.-X., Xie, F.-G., Yuan, F., et al. 2015, MNRAS, 447, 1692
Yuan, F., & Narayan, R. 2014, ARA&A, 52, 529
Zdziarski, A. A., Pjanka, P., Sikora, M., & Stawarz, Ł. 2014, MNRAS, 442, 3243

Appendix A: Observation log

Appendix B: Notes on individual sources

B.1. NGC 1566

NGC 1566 is a nearby CSAGN (z=0.00476), that showed multiple CS transitions over the years (see Jana et al. 2025, for details). More recently, NGC 1566 underwent an outburst in 2018 when the source transitioned from type 1.9 to type 1 states (e.g., Parker et al. 2019; Oknyansky et al. 2017, 2019). During this outburst, both primary continuum and soft excess flux increased along with optical, ultraviolet, mid-infrared, and millimeter fluxes (e.g., Oknyansky et al. 2019; Tripathi & Dewangan 2022). The source again moved back to type 2 state with fluxes in all wavebands gradually decreasing (Ochmann et al. 2020, 2024; Xu et al. 2024).

The X-ray properties of NGC 1566 has been studied extensively in the past (e.g., Kawamuro et al. 2013; Parker et al. 2019; Jana et al. 2021; Tripathi & Dewangan 2022). Previous studies have found an evolving SE that decreases when the flux decreases, consistent with the findings of the current work (e.g., Tripathi & Dewangan 2022). It is also found that reflection was very weak with $R_{\rm f} < 0.2$ (e.g., Jana et al. 2021). Modeling with RELXILLCP required an additional BLACKBODY component for the SE, indicating that ionized, blurred reflection is not the origin of the SE in this source, but rather warm Comptonization. Tripathi & Dewangan (2022) also found a similar result.

In the current work, we employed phenomenological models; however, our findings are consistent with previous studies that have examined the source in detail using physical models. Figure B.1 displays the relation of the SE with the continuum emission of NGC 1566. In our study, we found $\log(L_{\rm SE}^{0.5-2}/10^{42}) = (2.21 \pm 0.08)\log(L_{\rm PC}^{2-10}/10^{42}) - (1.33 \pm 0.09)$, with intrinsic scatter of 0.15 dex (1σ). The slope is steeper compared to the entire sample. The tight correlation of the SE and PC is consistent with the warm Comptonization scenario as the origin of the SE emission in NGC 1566.

We show the $\Gamma - \lambda_{\rm Edd}$ relation in Figure B.2. We obtained a V-shaped relation, with a break at $\log \lambda_{\rm Edd} = -2.58 \pm 0.09$, which is consistent with the entire sample. Figure B.3 shows the variation of Q as a function of $\lambda_{\rm Edd}$. The positive correlation indicates that the SE strongly deepens on the accretion rate, and SE emission vanishes rapidly at low-accretion state, possibly at $\log \lambda_{\rm Edd} < -2.5$. Both $Q - \lambda_{\rm Edd}$ and $\Gamma - \lambda_{\rm Edd}$ relations indicate the change of the accretion geometry at $\lambda_{\rm Edd} \sim 0.003$, below which the warm corona weakens significantly.

B.2. NGC 2617

NGC 2617 transitioned to type 1 state from type 2 state between 2003 and 2013 (Shappee et al. 2014). Since then, the source remained in type 1 state until 2023. In October 2023, NGC 2617 lost its broad Hβ line and entered a type 2 state (Oknyansky et al. 2023). NGC 2617 showed the presence of soft excess in 2013, when it was in the high-flux state (Giustini et al. 2017). Later the SE emission decreased as it moved toward the type 2 state.

NGC 2617 showed a strong positive correlation between the SE and continuum emission, with a Spearman correlation index of 0.95 with $p \ll 10^{-10}$. Figure B.4 shows the variation of the SE emission as a function of continuum emission. The linear fit between the two quantities revealed, $\log(L_{\rm SE}^{0.5-2}/10^{42}) = (1.89 \pm 0.07)\log(L_{\rm PC}^{2-10}/10^{42}) - (1.89 \pm 0.07)$. The observed slope is slightly steeper than that of the whole sample.

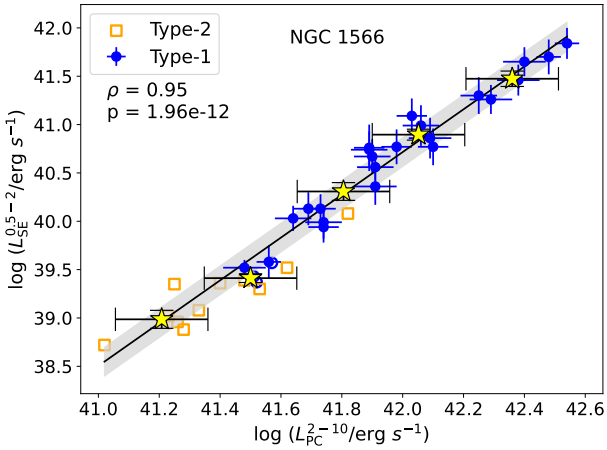

Fig. B.1. 0.5–2 keV soft excess luminosity ($L_{\rm SE}^{0.5-2}$) as a function of 2–10 keV primary continuum luminosity ($L_{\rm PC}^{2-10}$). The black solid line represents the linear best fit. The gray region marks the 1σ scatter.

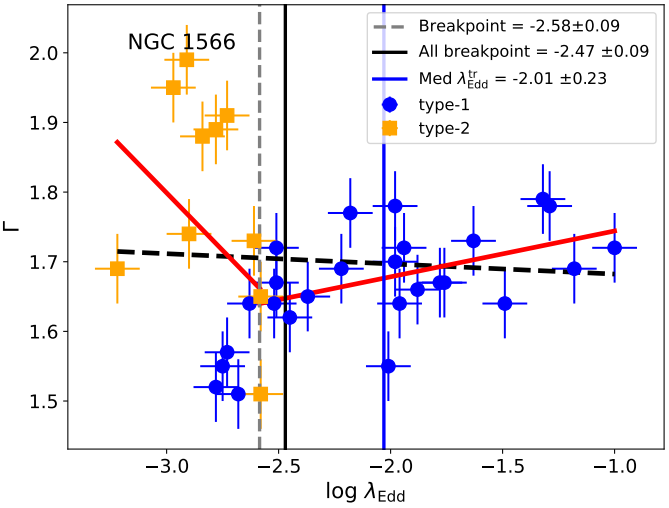

Fig. B.2. Relation between the photon index (Γ) and the Eddington ratio ($\lambda_{\rm Edd}$). The black dashed line represents the linear best fit. The two red lines represent the two-linear fit of the data, with a break. The vertical solid blue and solid black lines represent the median of transition Eddington ratio ($\lambda_{\rm Edd}^{\rm tr}$) and breakpoint for the entire sample, respectively. The gray dashed line represents the breakpoint for NGC 1566.

In Figure B.5, we show the relation between the Γ and $\lambda_{\rm Edd}$. The $\Gamma - \lambda_{\rm Edd}$ relation shows a sharp break at $\log \lambda_{\rm Edd} = -2.45 \pm 0.06$, indicating a change of geometry in the inner accretion flow. Figure B.6 displays the relation between the Q and $\lambda_{\rm Edd}$, which shows strong positive correlations, with $\rho = 0.87$ and $p \ll 10^{-10}$. The observed correlations among different parameters are consistent with the warm Comptonization scenario as the origin of the SE emission. The findings are also consistent with the entire sample.

We found that at $\log \lambda_{\rm Edd} \sim -2.5$, the SE emission diminishes very rapidly with decreasing accretion rate in NGC 2617. At the same $\lambda_{\rm Edd}$, the accretion geometry is also found to change. This suggests that the warm corona is closely linked with the inner accretion flow, possibly related to the inner accretion disk.

Table A.1. Observation log

Epochs	UT date (yyyy-mm-dd)	Soft X-ray instrument	Obs ID	Exp. (ks)	Hard X-ray instrument	Obs ID	Exp. (ks)	Type
			NGC 1566					
E1	2012-05-19	Suzaku/XIS	707002010	73	Suzaku/HXD	707002010	73	1.9
E2	2015-11-05	XMM	763500201	92	–	–	–	1.9
E3	2018-06-26	XMM	800840201	94	NuSTAR	80301601002	57	1
E4	2018-10-04	XMM	820530401	108	NuSTAR	80401601002	75	1
E5	2019-06-05	XMM	840800401	94	NuSTAR	80502606002	57	1
E6	2019-08-08	Swift/XRT	88910001	2	NuSTAR	60501031002	59	1
E7	2019-08-11	XMM	851980101	18	–	–	–	1
E8	2019-08-18	Swift/XRT	88910002	2	NuSTAR	60501031004	77	1
E9	2019-08-21	Swift/XRT	88910003	2	NuSTAR	60501031006	86	1
			NGC 2617					
E1	2013-04-27	XMM	701981601	35	–	–	–	1
E2	2013-05-24	XMM	701981901	66	–	–	–	1
			Mrk 590					
E1	2002-01-01	XMM	109130301	11	–	–	–	1
E2	2004-07-04	XMM	201020201	113	–	–	–	1
E3	2011-01-23	Suzaku/XIS	705043010	62	Suzaku/HXD	705043010	62	1
E4	2011-01-26	Suzaku/XIS	705043020	41	Suzaku/HXD	705043020	41	1
E5	2016-02-05	Swift/XRT	80903001	7	NuSTAR	60160095002	21	2
E6	2016-12-02	Swift/XRT	88014001	2	NuSTAR	90201043002	51	1
E7	2018-10-07	Swift/XRT	94095012	2	NuSTAR	80402610002	21	1
E8	2019-08-31	Swift/XRT	11542001	5	NuSTAR	80502630002	68	1
E9	2020-01-21	Swift/XRT	13172002	5	NuSTAR	80502630004	50	1
E10	2020-07-04	XMM	865470201	27	–	–	–	1
E11	2021-01-03	XMM	865470301	27	–	–	–	1
E12	2021-01-10	Swift/XRT	95662033	10	NuSTAR	80502630006	42	1
E13	2021-08-18	Swift/XRT	89297002	2	NuSTAR	60761012002	19	1
E14	2021-12-22	Swift/XRT	89297004	7	NuSTAR	80602604002	53	1
E15	2022-01-24	XMM	870840201	26				1
E16	2022-07-28	XMM	912400101	27				1
E17	2023-02-06	XMM	870840301	38	NuSTAR	80602604004	41	1
			Mrk 1018					
E1	2005-01-15	XMM	201090201	12	–	–	–	1
E2	2008-08-07	XMM	554920301	18	–	–	–	1
E3	2009-07-03	Suzaku/XIS	704044010	44	Suzaku/HXD	704044010	44	1
E4	2016-02-10	Swift/XRT	80898001	4	NuSTAR	60160087002	22	2
E5	2018-03-05	Swift/XRT	–	–	NuSTAR	60301022003	43	2
E6	2018-07-17	Swift/XRT	88207003	2	NuSTAR	60301022005	42	2
E7	2018-07-23	XMM	821240201	75	–	–	–	2
E8	2019-01-04	XMM	821240301	68	–	–	–	2
E9	2021-02-04	XMM	864350101	65	–	–	–	2
E10	2021-08-15	Swift/XRT	89296001	2	NuSTAR	60761011002	18	2
			IRAS 23226–3843					
E1	2016-07-08	Swift/XRT	81303001	6	NuSTAR	60160826002	22	1.8
E2	2017-05-02	XMM	760020101	16	–	–	–	1.9
E3	2017-06-11	XMM	760020401	86	NuSTAR	80101001002	97	1.9
E4	2019-11-07	XMM	840800501	90	NuSTAR	80502607002	55	1

Table B.1. Broadband X-ray properties of NGC 1566

Epoch	$\log L_{\rm PC}^{2-10}$	$\log L_{\rm SE}^{0.5-2}$	Γ	$E_{\rm cut}$ (keV)	$\log R_{\rm S}$	$kT_{\rm BB}$ (eV)	$\log Q$	$\log \lambda_{\rm Edd}$	χ^2/dof
(1)	(2)	(3)	(4)	(5)	(6)	(7)	(8)	(9)	(10)
E1	41.06 ± 0.01	< 39.22	1.96 ± 0.02	179^{+145}_{-109}	-0.37 ± 0.14	120*	< -2.03	-2.87 ± 0.05	538/422
E2	41.19 ± 0.03	39.60 ± 0.08	1.74 ± 0.03	200*	–	159 ± 9	-1.58 ± 0.09	-2.74 ± 0.06	1075/1000
E3	41.77 ± 0.02	40.49 ± 0.08	1.69 ± 0.02	90^{+30}_{-27}	-1.22 ± 0.48	134 ± 17	-1.28 ± 0.08	-2.13 ± 0.05	1570/1646
E4	42.01 ± 0.01	40.81 ± 0.10	1.69 ± 0.03	142^{+105}_{-78}	-1.09 ± 0.30	109 ± 12	-1.20 ± 0.10	-1.85 ± 0.05	715/663
E5	41.82 ± 0.01	40.42 ± 0.19	1.67 ± 0.03	200*	–	104 ± 39	-1.40 ± 0.19	-2.08 ± 0.05	838/833
E6	41.75 ± 0.01	40.35 ± 0.21	1.70 ± 0.04	174^{+119}_{-77}	-0.41 ± 0.21	117*	-1.40 ± 0.21	-2.15 ± 0.05	528/549
E7	41.81 ± 0.01	40.39 ± 0.22	1.69 ± 0.05	> 114	-1.00 ± 0.22	115*	-1.42 ± 0.22	-2.09 ± 0.05	558/567

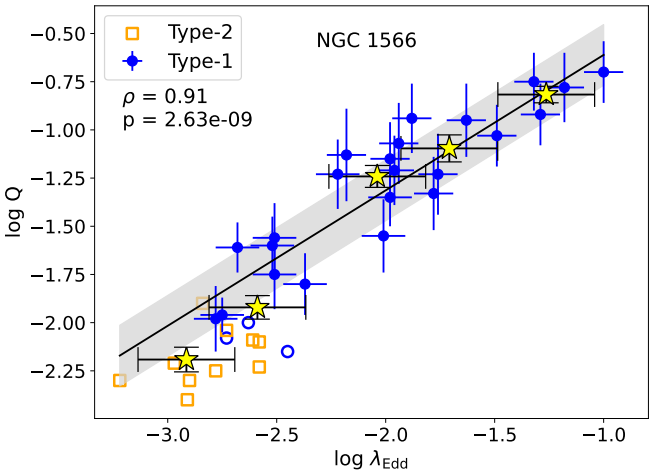

Fig. B.3. Variation of soft excess strength (Q) as a function of Eddington ratio ($\lambda_{\rm Edd}$). The black solid line represents the linear best fit. The gray region marks the 1σ scatter.

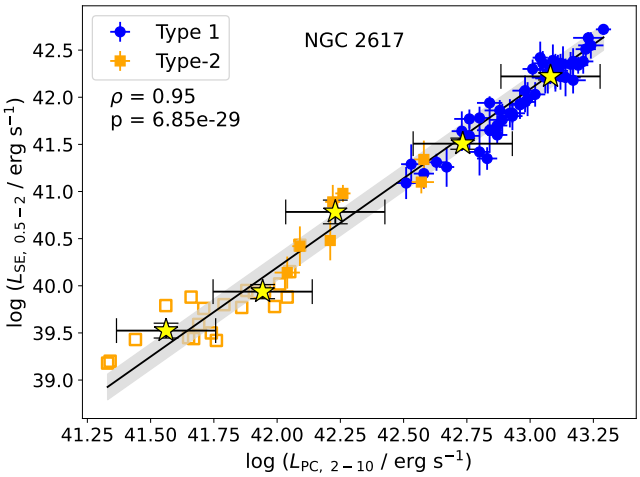

Fig. B.4. 0.5–2 keV soft excess luminosity ($L_{\rm SE}^{0.5-2}$) as a function of 2–10 keV primary continuum luminosity ($L_{\rm PC}^{2-10}$). The black solid line represents the linear best fit. The gray region marks the 1σ scatter.

Once the inner accretion disk receded, the warm corona also became weak.

B.3. Mrk 590

Mrk 590 showed several CS transitions in the past four decades (e.g., Denney et al. 2014; Jana et al. 2025). The source entered a type 2 state in 2006 (Denney et al. 2014), where it remained until 2014. After that, the flux slowly increased, and the source entered a type 1 state in 2017 (Oh et al. 2022). The broadband X-ray properties of Mrk 590 have been studied extensively in the past (e.g., Rivers et al. 2012; Ghosh et al. 2022; Lawther et al. 2023). Mrk 590 showed a variable SE emission, where the SE generally weakens when the primary flux decreases (e.g., Ghosh et al. 2022). Rivers et al. (2012) found that the SE emission decreased by a factor of $\sim 20-30$, while the PC emission only changed about $\sim 10\%$, suggesting the SE emission is independent of the PC emission. Ghosh et al. (2022) found that SE emission could be explained with both ionized reflection and warm Comptonization scenarios. Palit et al. (2025) reported the emergence of the SE emission when the source transitioned to a type 1 state, when the UV flux also increased. The authors suggested that it is linked with the warm corona, which forms or becomes strong with increasing accretion rate.

Figure B.7 displays the relation between the SE emission and the continuum emission. The SE emission has a strong positive correlation with the continuum emission with $\rho = 0.90$ and $p \ll 10^{-10}$. With linear fitting, we obtained $\log(L_{\rm SE}^{0.5-2}/10^{42}) = (1.69 \pm 0.15) \log(L_{\rm PC}^{2-10}/10^{42}) - (1.88 \pm 0.18)$, with an intrinsic scatter of 0.19 dex (1σ).

We show the relation between the Γ and $\lambda_{\rm Edd}$ in Figure B.8. We obtained a positive correlation between these two parameters. Figure B.9 shows the variation of Q as a function of $\lambda_{\rm Edd}$. We obtained a positive correlation with $\rho = 0.65$ and $p < 10^{-5}$. Broadband spectral analysis revealed the reflection is very weak or absent, suggesting the reflection did not contribute to the SE emission. The correlations we obtained among different parameters indicate that the origin of the SE emission is most probably the warm corona.

In Mrk 590, we did not observe any change of geometry in the inner accretion flow, although there is a hint of change in slope at $\log \lambda_{\rm Edd} < -1.5$. We also obtained only an upper limit of the SE flux below $\log \lambda_{\rm Edd} \sim -2$, indicating the warm corona substantially weakens below this.

Table B.2. Broadband X-ray properties of NGC 2617

Epoch	$\log L_{\rm PC}^{2-10}$	$\log L_{\rm SE}^{0.5-2}$	Γ	$E_{\rm cut}$ (keV)	$\log R_{\rm S}$	$kT_{\rm BB}$ (eV)	$\log Q$	$\log \lambda_{\rm Edd}$	χ^2/dof
(1)	(2)	(3)	(4)	(5)	(6)	(7)	(8)	(9)	(10)
E1	42.97 ± 0.03	41.89 ± 0.07	1.78 ± 0.03	200*	–	125 ± 8	-1.08 ± 0.08	-1.21 ± 0.09	1596/1439
E2	43.21 ± 0.03	42.19 ± 0.11	1.96 ± 0.03	200*	–	99 ± 14	-1.02 ± 0.11	-0.91 ± 0.09	1435/1314
E3	42.00 ± 0.21	< 41.11	2.09 ± 0.14	200*	–	120*	< -0.89	-2.31 ± 0.22	59/63

Table B.3. Broadband X-ray properties of Mrk 590

Epoch	$\log L_{\rm PC}^{2-10}$	$\log L_{\rm SE}^{0.5-2}$	Γ	$E_{\rm cut}$ (keV)	$\log R_{\rm S}$	$kT_{\rm BB}$ (eV)	$\log Q$	$\log \lambda_{\rm Edd}$	χ^2/dof
(1)	(2)	(3)	(4)	(5)	(6)	(7)	(8)	(9)	(10)
E1	42.80 ± 0.02	41.13 ± 0.11	1.62 ± 0.04	200*	–	157 ± 29	-1.67 ± 0.11	-1.71 ± 0.05	157/169
E2	42.89 ± 0.01	41.17 ± 0.12	1.69 ± 0.04	200*	–	129 ± 13	-1.72 ± 0.12	-1.61 ± 0.05	679/666
E3	42.96 ± 0.01	< 41.34	1.67 ± 0.04	> 65	-0.82 ± 0.10	120*	< -1.62	-1.52 ± 0.05	831/754
E4	42.94 ± 0.01	< 41.36	1.67 ± 0.03	> 58	-0.89 ± 0.12	120*	< -1.58	-1.55 ± 0.05	480/445
E5	42.53 ± 0.02	< 40.56	1.65 ± 0.03	> 75	-0.70 ± 0.08	120*	< -1.97	-2.01 ± 0.05	435/465
E6	42.61 ± 0.02	< 40.66	1.72 ± 0.04	> 63	-0.57 ± 0.07	120*	< -1.95	-1.92 ± 0.05	385/447
E7	43.12 ± 0.01	< 41.49	1.73 ± 0.04	72^{+39}_{-24}	-2.00 ± 0.60	120*	< -1.63	-1.34 ± 0.05	569/684
E8	43.33 ± 0.02	41.80 ± 0.19	1.82 ± 0.02	60^{+25}_{-17}	-0.15 ± 0.10	152 ± 58	-1.53 ± 0.19	-1.08 ± 0.05	1271/1287
E9	43.31 ± 0.01	41.72 ± 0.21	1.83 ± 0.04	55^{+24}_{-14}	-1.13 ± 0.15	124 ± 36	-1.59 ± 0.21	-1.10 ± 0.05	1160/1211
E10	42.93 ± 0.01	41.33 ± 0.25	1.75 ± 0.03	200*	–	166 ± 30	-1.60 ± 0.25	-1.56 ± 0.05	630/628
E11	43.03 ± 0.01	41.45 ± 0.21	1.64 ± 0.02	200*	–	153 ± 18	-1.58 ± 0.21	-1.44 ± 0.05	659/678
E12	43.01 ± 0.01	< 41.14	1.62 ± 0.02	66^{+20}_{-16}	-0.80 ± 0.10	120*	< -1.87	-1.47 ± 0.05	947/1001
E13	43.32 ± 0.01	< 41.68	1.91 ± 0.02	59^{+21}_{-11}	-0.14 ± 0.11	120*	< -1.64	-1.09 ± 0.05	694/761
E14	42.91 ± 0.02	< 41.33	1.73 ± 0.04	> 54	-0.64 ± 0.14	120*	< -1.58	-1.58 ± 0.05	894/947
E15	42.48 ± 0.02	< 40.97	1.76 ± 0.03	200*	–	120*	< -1.51	-2.07 ± 0.05	348/342
E16	42.91 ± 0.02	41.25 ± 0.19	1.68 ± 0.05	200*	–	154 ± 18	-1.66 ± 0.19	-1.58 ± 0.05	580/593
E17	42.85 ± 0.02	41.11 ± 0.17	1.61 ± 0.02	> 88	-1.06 ± 0.13	152 ± 12	-1.74 ± 0.17	-1.65 ± 0.05	1104/1141

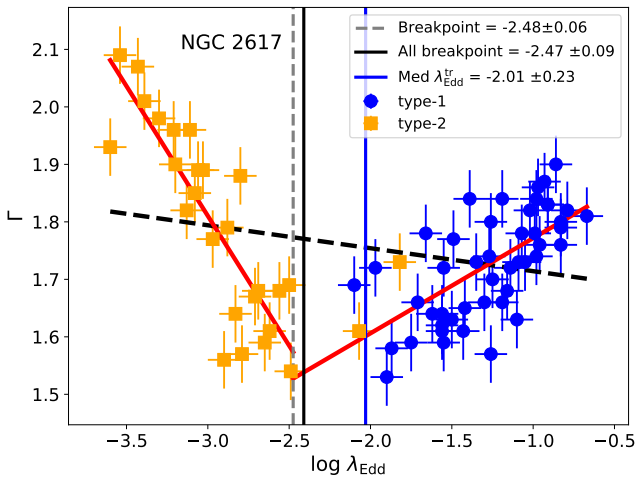

Fig. B.5. Relation between the photon index (Γ) and the Eddington ratio ($\lambda_{\rm Edd}$). The black dashed line represents the linear best fit. The two red lines represent the two-linear fit of the data, with a break. The vertical solid blue and solid black lines represent the median of transition Eddington ratio ($\lambda_{\rm Edd}^{\rm tr}$) and breakpoint for the entire sample, respectively. The gray dashed line represents the breakpoint for NGC 2617.

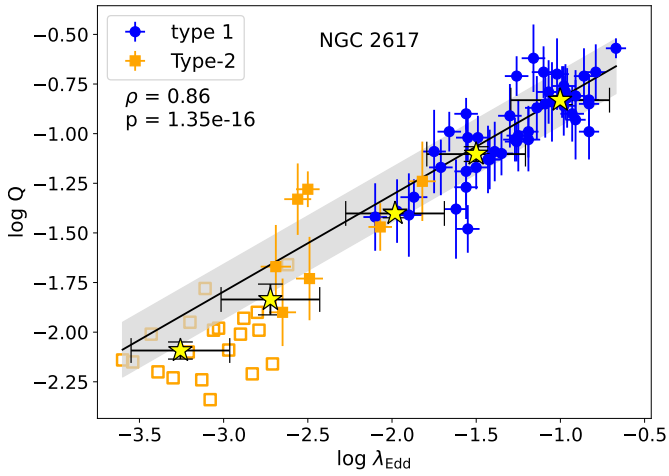

Fig. B.6. Variation of soft excess strength (Q) as a function of Eddington ratio ($\lambda_{\rm Edd}$). The black solid line represents the linear best fit. The gray region marks the 1σ scatter.

B.4. Mrk 1018

Mrk 1018 is one of the first AGNs that showed CS transitions (Cohen et al. 1986). The source transitioned to type 1 state in 1984, where it remained until 2008 (McElroy et al. 2016). The source moved to type 1.9 state in January 2015 (McElroy et al. 2016). In 2020, the source showed a full CS transition when it

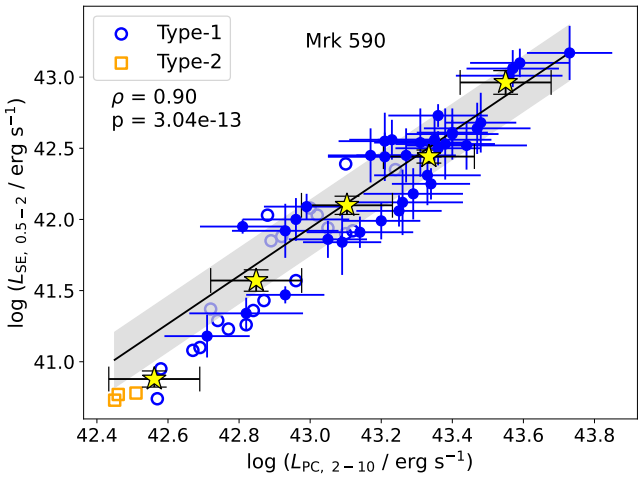

Fig. B.7. 0.5–2 keV soft excess luminosity ($L_{\rm SE}^{0.5-2}$) as a function of 2–10 keV primary continuum luminosity ($L_{\rm PC}^{2-10}$). The black solid line represents the linear best fit. The gray region marks the 1σ scatter.

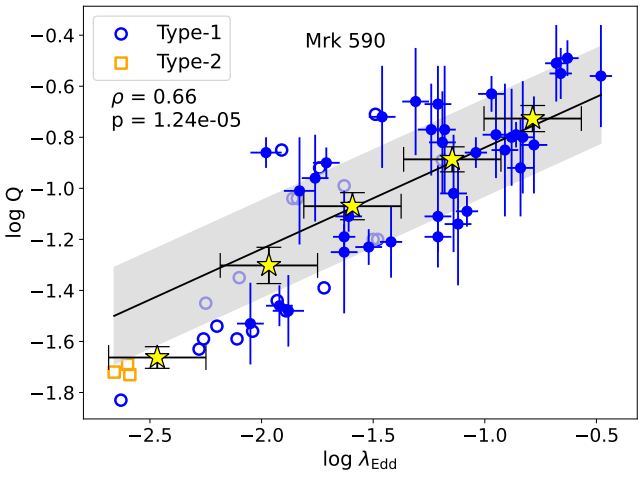

Fig. B.9. Variation of soft excess strength (Q) as a function of Eddington ratio ($\lambda_{\rm Edd}$). The black solid line represents the linear best fit. The gray region marks the 1σ scatter.

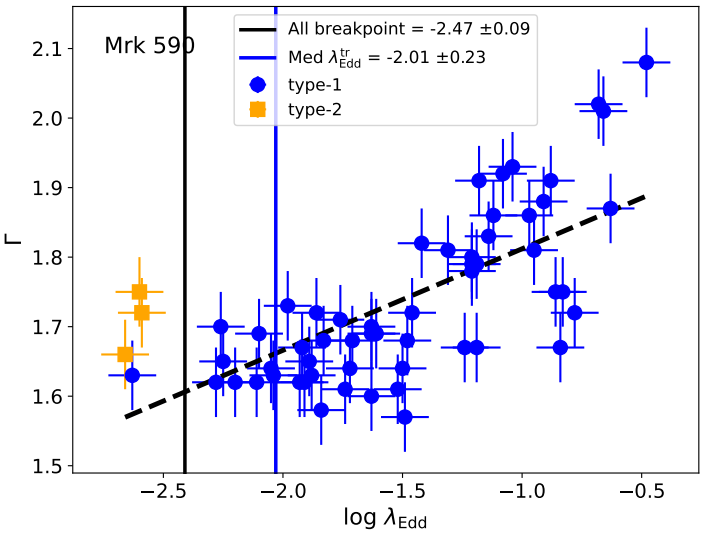

Fig. B.8. Relation between the photon index (Γ) and the Eddington ratio ($\lambda_{\rm Edd}$). The black dashed line represents the linear best fit. The vertical solid blue and solid black lines represent the median of transition Eddington ratio ($\lambda_{\rm Edd}^{\rm tr}$) and breakpoint for the entire sample, respectively.

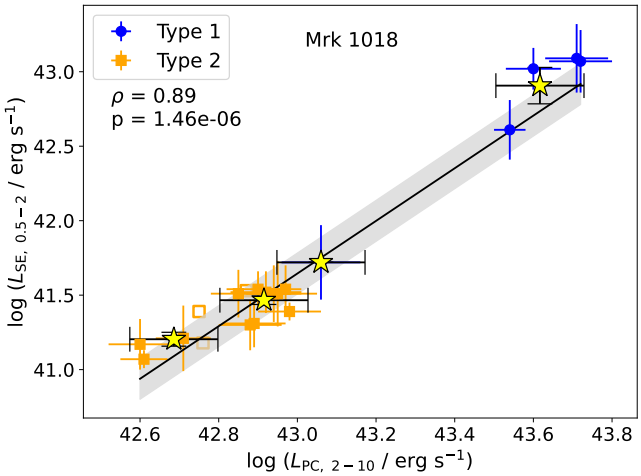

Fig. B.10. 0.5–2 keV soft excess luminosity ($L_{\rm SE}^{0.5-2}$) as a function of 2–10 keV primary continuum luminosity ($L_{\rm PC}^{2-10}$). The black solid line represents the linear best fit. The gray region marks the 1σ scatter.

briefly entered a type 1 state and moved back to type 1.8 state (Lu et al. 2025).

The broadband X-ray properties of Mrk 1018 have been studied extensively in the past (e.g., Noda & Done 2018; Lyu et al. 2021; Veronese et al. 2024), which agrees with our findings. We find that the reflection is very weak or absent in the broadband X-ray spectroscopy. This agrees with the work of Veronese et al. (2024), who found that no reflection component is needed to model the hard X-ray spectra. We also found evolving SE emission, which is also reported in the previous studies (e.g., Noda & Done 2018). These suggest that warm coronal emission contributes to the SE emission in Mrk 1018.

Figure B.10 displays the relation between the SE and continuum emission of Mrk 1018. Strong positive relation ($\rho = 0.89$ and $p < 10^{-5}$.) suggests a common physical origin of the SE and continuum emission. In Figure B.11, we show the relation between Γ and $\lambda_{\rm Edd}$. We obtained a positive correlation between these two parameters, with a hint of break around $\log \lambda_{\rm Edd} \sim -2.5$. Figure B.12 shows the variation of Q with $\lambda_{\rm Edd}$. We obtained $\rho = 0.71$ and $p < 10^{-5}$, indicating Q strongly linked with the accretion rate.

In Mrk 1018, we could only probe up to $\log \lambda_{\rm Edd} \sim -2.7$. Low SE emission indicates that the warm corona becomes weak at this $\lambda_{\rm Edd}$, and still exists. We expect the warm corona would vanish or diminish at lower $\lambda_{\rm Edd}$. The observed relations among different parameters are consistent with the warm corona scenario of the SE.

B.5. IRAS 23226–3843

IRAS 23226–3843 showed several CS transitions in the last decade (e.g., Kollatschny et al. 2020, 2023; Jana et al. 2025).

Table B.4. Broadband X-ray properties of Mrk 1018

Epoch	$\log L_{\rm PC}^{2-10}$	$\log L_{\rm SE}^{0.5-2}$	Γ	$E_{\rm cut}$ (keV)	$\log R_{\rm S}$	$kT_{\rm BB}$ (eV)	$\log Q$	$\log \lambda_{\rm Edd}$	χ^2/dof
(1)	(2)	(3)	(4)	(5)	(6)	(7)	(8)	(9)	(10)
E1	43.57 ± 0.03	42.61 ± 0.16	1.84 ± 0.04	200*	–	108 ± 27	-0.96 ± 0.16	-1.08 ± 0.06	194/217
E2	43.67 ± 0.02	42.70 ± 0.14	1.87 ± 0.03	200*	–	127 ± 10	-0.97 ± 0.14	-0.95 ± 0.05	684/684
E3	43.51 ± 0.02	42.55 ± 0.13	1.77 ± 0.04	> 77	–	120*	-0.96 ± 0.13	-1.15 ± 0.05	667/589
E4	42.72 ± 0.03	< 40.89	1.65 ± 0.05	> 98	-0.76 ± 0.15	120*	< -1.83	-2.07 ± 0.06	165/219
E5	42.83 ± 0.03	< 41.35	1.62 ± 0.04	> 105	-1.11 ± 0.18	120*	< -1.48	-1.95 ± 0.06	208/219
E6	42.75 ± 0.02	–	1.69 ± 0.04	> 91	-1.10 ± 0.14	–	–	-2.03 ± 0.05	166/161
E7	42.80 ± 0.03	< 41.52	1.63 ± 0.05	> 108	-1.07 ± 0.13	120*	< -1.28	-1.98 ± 0.06	213/274
E8	42.91 ± 0.02	41.51 ± 0.08	1.64 ± 0.03	200*	–	127 ± 36	-1.40 ± 0.08	-1.86 ± 0.05	664/637
E9	42.57 ± 0.02	41.29 ± 0.06	1.70 ± 0.03	200*	–	125 ± 35	-1.28 ± 0.06	-2.23 ± 0.05	393/409
E10	42.57 ± 0.02	41.25 ± 0.05	1.69 ± 0.03	200*	–	129 ± 37	-1.32 ± 0.05	-2.23 ± 0.05	416/404
E11	42.71 ± 0.02	< 41.62	1.62 ± 0.04	> 122	-2.08 ± 0.34	120*	< -1.09	-2.08 ± 0.05	80/117

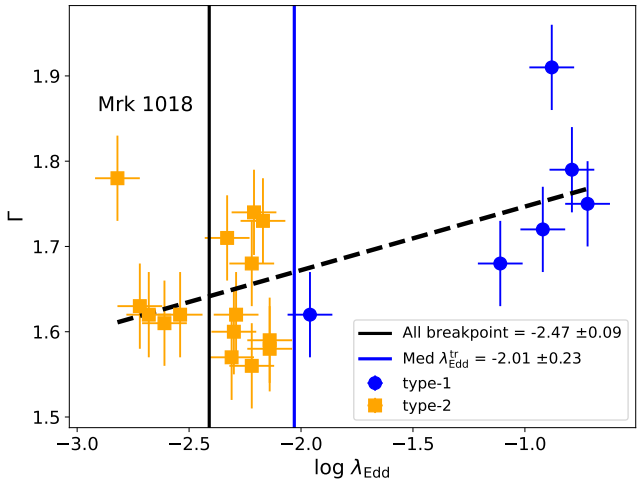

Fig. B.11. Relation between the photon index (Γ) and the Eddington ratio ($\lambda_{\rm Edd}$). The black dashed line represents the linear best fit. The vertical solid blue and solid black lines represent the median of transition Eddington ratio ($\lambda_{\rm Edd}^{\rm tr}$) and breakpoint for the entire sample, respectively.

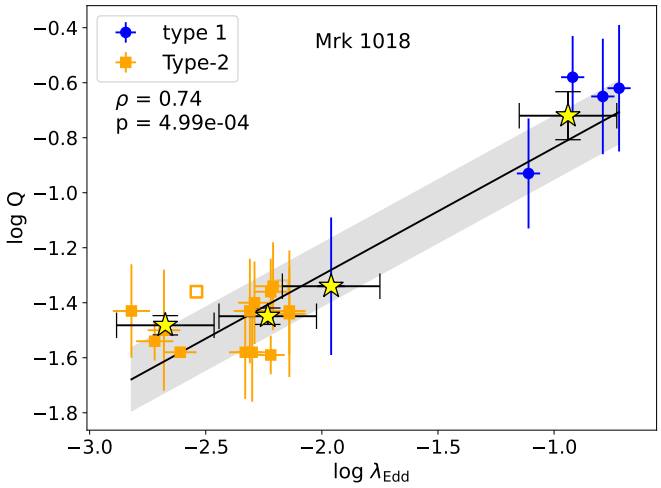

Fig. B.12. Variation of soft excess strength (Q) as a function of Eddington ratio ($\lambda_{\rm Edd}$). The black solid line represents the linear best fit. The gray region marks the 1σ scatter.

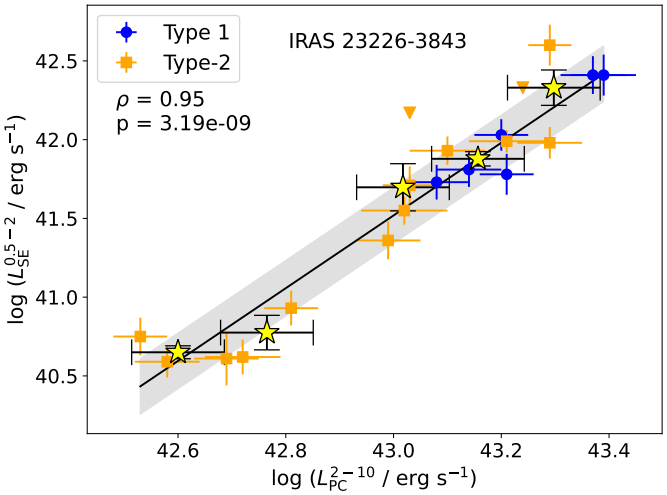

Fig. B.13. 0.5–2 keV soft excess luminosity ($L_{\rm SE}^{0.5-2}$) as a function of 2–10 keV primary continuum luminosity ($L_{\rm PC}^{2-10}$). The black solid line represents the linear best fit. The gray region marks the 1σ scatter.

We detected SE emission in the source, which evolves with the accretion rate. Figure B.13 shows the relation of the SE and continuum emission, which shows a strong positive correlation with $\rho = 0.95$ and $p < 10^{-5}$. We find the presence of moderate reflection in the source; however, the strength of the Compton hump (reflection strength R_S) does not correlate with the Q. This suggests that the SE originates from a warm Corona.

Figure B.14 displays the relation between Γ and $\lambda_{\rm Edd}$. The $\Gamma-\lambda_{\rm Edd}$ shows a V-shaped relation with a break at $\log \lambda_{\rm Edd} \sim -2.1$, indicating a possible change of inner accretion flow. Figure B.15 shows the variation of Q as a function of $\lambda_{\rm Edd}$. A positive correlation between these two parameters indicates that SE emission is strongly linked with the accretion rate. These relations are consistent with the warm Comptonization scenario as the origin of the SE.

Appendix C: Soft excess model

We modeled SE emission using a phenomenological blackbody (BB) model. We chose this model as we wanted to test both warm corona and ionized reflection scenarios as the origin of the

Table B.5. Broadband X-ray properties of IRAS 23226–3843

Epoch	$\log L_{\rm PC}^{2-10}$	$\log L_{\rm SE}^{0.5-2}$	Γ	$E_{\rm cut}$ (keV)	$\log R_{\rm S}$	$kT_{\rm BB}$ (eV)	$\log Q$	$\log \lambda_{\rm Edd}$	χ^2/dof
(1)	(2)	(3)	(4)	(5)	(6)	(7)	(8)	(9)	(10)
E1	42.49 ± 0.06	< 41.14	1.89 ± 0.03	> 51	-0.44 ± 0.09	120^{*}	-1.35 ± 0.06	-2.34 ± 0.08	158/201
E2	42.10 ± 0.03	< 41.10	1.94 ± 0.05	200^{*}	–	120^{*}	< -1.00	-2.74 ± 0.06	86/85
E3	42.02 ± 0.03	41.03 ± 0.43	2.04 ± 0.03	> 55	-1.74 ± 0.19	112 ± 19	-0.99 ± 0.43	-2.82 ± 0.06	157/168
E4	43.10 ± 0.01	42.06 ± 0.14	1.91 ± 0.02	136^{+99}_{-84}	-0.40 ± 0.09	133 ± 13	-1.04 ± 0.14	-1.66 ± 0.05	1569/1489

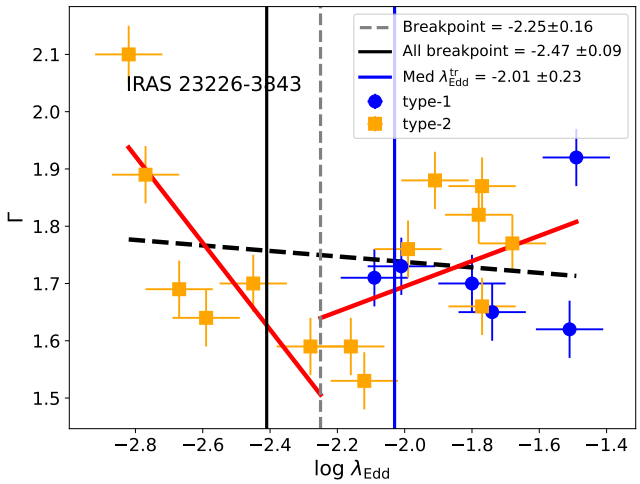

Fig. B.14. Relation between the photon index (Γ) and the Eddington ratio ($\lambda_{\rm Edd}$). The black dashed line represents the linear best fit. The two red lines represent the two-linear fit of the data, with a break. The vertical solid blue and solid black lines represent the median of transition Eddington ratio ($\lambda_{\rm Edd}^{\rm tr}$) and breakpoint for the entire sample, respectively. The gray dashed line represents the breakpoint for IRAS 23226–3843.

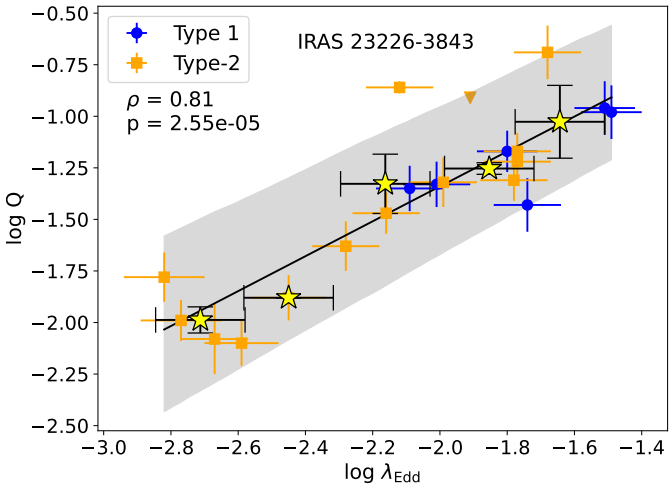

Fig. B.15. Variation of soft excess strength (Q) as a function of Eddington ratio ($\lambda_{\rm Edd}$). The black solid line represents the linear best fit. The gray region marks the 1σ scatter.

SE. We note that in warm Comptonization scenario, a Comptonization model such as COMPTT or NTHCOMP would provide a more physical description of the SE emission. To test this, we replaced the blackbody component with NTHCOMP and found that the flux in the 0.5–2 keV range remains unchanged. However, when integrating over the broader 0.001–10 keV range, NTHCOMP yields fluxes higher by ∼0.2 dex compared to the blackbody model. This difference does not significantly affect $L_{\rm bol}$, as the bulk of the emission originates from the DISKBB and power-law components.